nature communications

Article

https://doi.org/10.1038/s41467-024-52158-z

Merging semi-crystallization and multispecies iodine intercalation at photo-redox interfaces for dual high-value synthesis

Received: 16 March 2024

Accepted: 27 August 2024

Published online: 06 September 2024

Check for updates

Fei Chen[1,4] ✉, Chang-Wei Bai[1,4], Pi-Jun Duan[1,4], Zhi-Quan Zhang[1], Yi-Jiao Sun[1], Xin-Jia Chen[1], Qi Yang[2] & Han-Qing Yu[3] ✉

The artificial photocatalytic synthesis based on graphitic carbon nitride (g-C_3N_4) for H_2O_2 production is evolving rapidly. However, the simultaneous production of high-value products at electron and hole sites remains a great challenge. Here, we use transformable potassium iodide to obtain semi-crystalline g-C_3N_4 integrated with the I^-/I_3^- redox shuttle mediators for efficient generation of H_2O_2 and benzaldehyde. The system demonstrates a prominent catalytic efficiency, with a benzaldehyde yield of 0.78 mol g^{-1} h^{-1} and an H_2O_2 yield of 62.52 mmol g^{-1} h^{-1}. Such a constructed system can achieve an impressive 96.25% catalytic selectivity for $2e^-$ oxygen reduction, surpassing previously reported systems. The mechanism study reveals that the strong crystal electric field from iodized salt enhances photo-generated charge carrier separation. The I^-/I_3^- redox mediators significantly boost charge migration and continuous electron and proton supply for dual-channel catalytic synthesis. This groundbreaking work in photocatalytic co-production opens neoteric avenues for high-value synthesis.

The utilization of hydrogen peroxide (H_2O_2) as an effective and eco-friendly energy vector in domains such as medicine, chemical industry, and biology is experiencing a consistent upsurge[1]. This increasing demand necessitates alternative methodologies to the traditional yet energetically intensive and waste-generating anthraquinone process[2]. Implementing artificial photosynthesis for H_2O_2 from water and oxygen, which translates inexhaustible solar energy into storable chemical forms, marks a substantial advancement in the energy transition[3,4]. Significant progress has been made in developing H_2O_2 photosynthesis, though numerous challenges impede its application. For instance, the lethargic kinetics of the water oxidation half-reaction contributed to a deficient proton supply, critically hindering the efficiency of the photocatalytic oxygen reduction reaction (ORR)[5,6]. Conventionally, sacrificial agents like triethanolamine and isopropanol, among other small organic molecules, have been utilized to circumvent water oxidation reaction (WOR)[7–9]. Their inclusion enhanced proton availability and mitigated the recombination of electrons and holes. While the introduction of sacrificial agents significantly accelerated H_2O_2 production, the generation of essentially valueless oxidative by-products led to the unproductive expenditure of photo-generated hole energy[10,11].

Nonetheless, relentless global research efforts have culminated in the advent of a novel trend: the photosynthesis of H_2O_2 concurrent with the parallel generation of high-value organic compounds, thereby optimizing photon and atom utilization[12]. A key oxidation product in this process, the conversion of benzyl alcohol (BzOH) to benzaldehyde (BA), holds significant value as an intermediate in the synthesis of fragrances and pharmaceuticals[13]. Moreover, the biphasic system

[1]Key Laboratory of the Three Gorges Reservoir Region's Eco-Environment, Ministry of Education, College of Environment and Ecology, Chongqing University, Chongqing 400045, China. [2]Key Laboratory of Environmental Biology and Pollution Control, Ministry of Education, College of Environmental Science and Engineering, Hunan University, Changsha 410082, China. [3]CAS Key Laboratory of Urban Pollutant Conversion, Department of Environmental Science and Engineering, University of Science and Technology of China, Hefei 230026, China. [4]These authors contributed equally: Fei Chen, Chang-Wei Bai, Pi-Jun Duan. ✉e-mail: fchen0505@cqu.edu.cn; hqyu@ustc.edu.cn

comprising BzOH and water facilitates the separation of H_2O_2 and other potential active substances during the reaction, safeguarding the catalyst against oxidative degradation[14]. With an oxidation potential lower than WOR, BzOH emerged as an advantageous organic substrate[15]. Consequently, the shift towards a more efficient photocatalytic coupled production approach necessitates advanced multifunctional catalyst designs.

Graphitic carbon nitride (g-C_3N_4, CN) has garnered considerable attention in photocatalytic synthesis, attributed to its cost-effectiveness, stability, and structural tunability[16,17]. Nonetheless, the intrinsic slow surface reaction kinetics and pronounced charge carrier recombination in unmodified CN substantially constrain its photocatalytic efficiency[18,19]. Crystal engineering, promoting the formation of a robust built-in electric field, has emerged as a potent approach to augment CN's inherent photocatalytic properties[20,21]. This highly organized structural configuration enhanced the dissociation of photo-generated carriers and improved charge transfer from bulk to surface[22]. Moreover, strategies encompassing surface modifications or elemental doping within the ambit of crystal engineering could further escalate photocatalytic activity, thereby potentially revolutionizing photocatalytic performance.

A prevalent method for synthesizing crystalline CN involved the utilization of a LiCl/KCl eutectic salt as both a solvent and a template[23–25]. This approach notably expedited the deammoniation process, which in return diminished the interlayer spacing and fostered the migration of photo-generated charge carriers, culminating in enhanced photocatalytic activity. Prior studies have demonstrated that employing a KI/KCl mixed salt during calcination can produce *semi*-crystalline CN, significantly outperforming pristine CN in photocatalytic H_2O_2 production[26]. Observations indicated that various potassium salt combinations improve CN crystallinity. Notably, specific transformable salts like KI could induce the formation of a KI/KI_3 mixed salt, suggesting their potential as versatile options in molten salt templates. In recent discussions, the I^-/I_3^- redox shuttle mediator has been recognized for its stable and efficient electron transfer capabilities, particularly in applications like battery development and water splitting[27,28]. The integration of eutectic salts that not only enhanced CN's crystallinity but also embed I^-/I_3^- redox shuttle mediator into the structure represented a synergistic strategy. Thus, a combined modification approach, incorporating both crystalline engineering and the integration of the I^-/I_3^- redox mediators, is poised to significantly advance the capabilities of CN, particularly for both ORR and selective alcohol oxidation. Simultaneously, we anticipate that incorporating various iodine species will reinforce the iodine's stability between CN layers and consistently yield high-value products over time. Nevertheless, the facile preparation of CN with this dual-functional efficiency remains a complex challenge. Also, it is required to elucidate the impact of these dual-benefit strategies on the overall photocatalytic performance.

As anticipated, a KI/KI_3 mixed eutectic salt, synthesized from post-site insertion by combining KI and I_2, facilitated the creation of high-crystallinity CN (CN-I/I_3) embedded with I^-/I_3^- redox mediators through a facile two-step calcination (Fig. 1a). The implementation of this dual-modification strategy significantly augmented the photocatalytic efficiency of CN-I/I_3. Notably, an impressive H_2O_2 generation rate of 62.52 mmol g^{-1} h^{-1} (with a high selectivity of 96.62%) could be achieved at the conduction band (CB) reduction platform and a benzaldehyde production rate of 0.78 mol g^{-1} h^{-1} (selectivity of 92.65%) on the oxidation platform of valance band (VB). Advanced diagnostic methodologies, such as in situ diffuse reflectance infrared Fourier-transform spectroscopy (DRIFTS), femtosecond transient absorption spectroscopy (*fs*-TAS), Kelvin probe force microscopy (KPFM), and theoretical simulations, supported the conclusion that the increased crystallinity and the resulting robust built-in electric field significantly enhance the separation of photo-generated carriers. Incorporating I^-/I_3^- redox mediators could effectively improve the transfer and mobility of these carriers, supplying enough electrons and protons. Notably, under natural sunlight, the concentration of H_2O_2 reached 158.48 mM after 8 h. CN-I/I_3 also exhibited its versatility under various complex conditions. This study sets a neoteric precedent in developing efficient CN-based photocatalysts and presents a viable method for co-producing high-value chemicals, optimizing atom-economical utilization by employing electrons and holes in separate reactions.

Results

Phenomenon identification–theoretical prediction–activity evaluation

Observations revealed that the decomposition of potassium iodide, mainly when used for an extended period, could occur (Supplementary Fig. 2a). Integrating these decomposed components into the g-C_3N_4 (CN) matrix drastically enhanced its catalytic performance (Supplementary Fig. 2b, c). A vital aspect of this improved performance was the formation of I_3^-, predominantly attributed to incorporating I_2 (Supplementary Fig. 2a). Drawing inspiration from these findings, various amounts of I_2 were introduced into the CN system. This addition aimed to simulate the metathesis process and facilitate the forming of intercalated layers comprising I^-/I_3^- redox mediators, potentially enhancing the photocatalytic efficacy.

To elucidate the impact and functionality of I^- or I_3^- species as redox mediators in subsequent high-value chemical reactions, this study established three distinct model systems: the original CN, CN co-polymerized with KI (termed CN-I), and CN co-polymerized with a KI/I_2 mixture (CN-I/I_3) (Fig. 2a–c, Supplementary Fig. 3 and Supplementary Data 1). A comprehensive investigation utilizing density of states (DOS) analyses was conducted to assess the influence of I^- or I_3^- incorporation on the electronic band structure and band gap of CN (Fig. 1e–g). The valence band (VB) of unmodified CN predominantly consisted of N's 2p orbitals, while its conduction band (CB) was chiefly composed of the 2p orbitals of C and N. Integration of I^- the CN matrix led to the emergence of mid-gap states within the CB, causing a downward shift in the CB edge and narrowing the band gap. In contrast, introducing I_3^- elicited an upward shift in CN's VB. Notably, CN co-polymerized with both I^- and I_3^- (CN-I/I_3) exhibited the most significant reduction in the band gap. This narrower band gap enhanced visible light absorption and improved the driving force for ORR.

Theoretical calculations revealed surface work functions for CN, CN-I, and CN-I/I_3 as 5.150, 4.254, and 4.168 eV, respectively (Fig. 1d, h, l). Incorporating I^- and the combined I^-/I_3^- systems could result in a progressive elevation of the Fermi level, easing the constraints on free electron movement and concurrently reducing the work function. These changes suggested that the addition of I^- or I_3^- facilitated the migration of photo-generated electrons, thereby increasing surface reaction rates[29]. The synergistic effect was more pronounced with the simultaneous introduction of I^- and I_3^-. Furthermore, electrostatic potential (ESP) analyses and two-dimensional electron density mapping were used to investigate the charge distribution characteristics in CN post I^- or I_3^- (Fig. 1b, c). While electronegative atoms presented negative electrostatic potential and conjugated surfaces displayed positive potential, creating electron-rich and electron-deficient areas, the symmetric structure of pristine CN led to a uniformly distributed charge, impeding charge transfer. The inclusion of I^- or I^-/I_3^- disrupted such uniformity, promoting charge separation. Furthermore, optical property evaluations based on a six-flux model indicated that CN-I/I_3 showed better characteristics compared to CN and CN-I, implying enhanced photoactivity (Supplementary Fig. 4; Supplementary Tables 1 and 2). These findings confirm that embedding I^- or I_3^- boosted light absorption and charge separation efficiency in CN.

Taking into account the aforementioned considerations, we developed a dual high-value conversion system to validate the innovative design of the catalyst. In photocatalytic H_2O_2 production, benzyl

https://doi.org/10.1038/s41467-024-52158-z

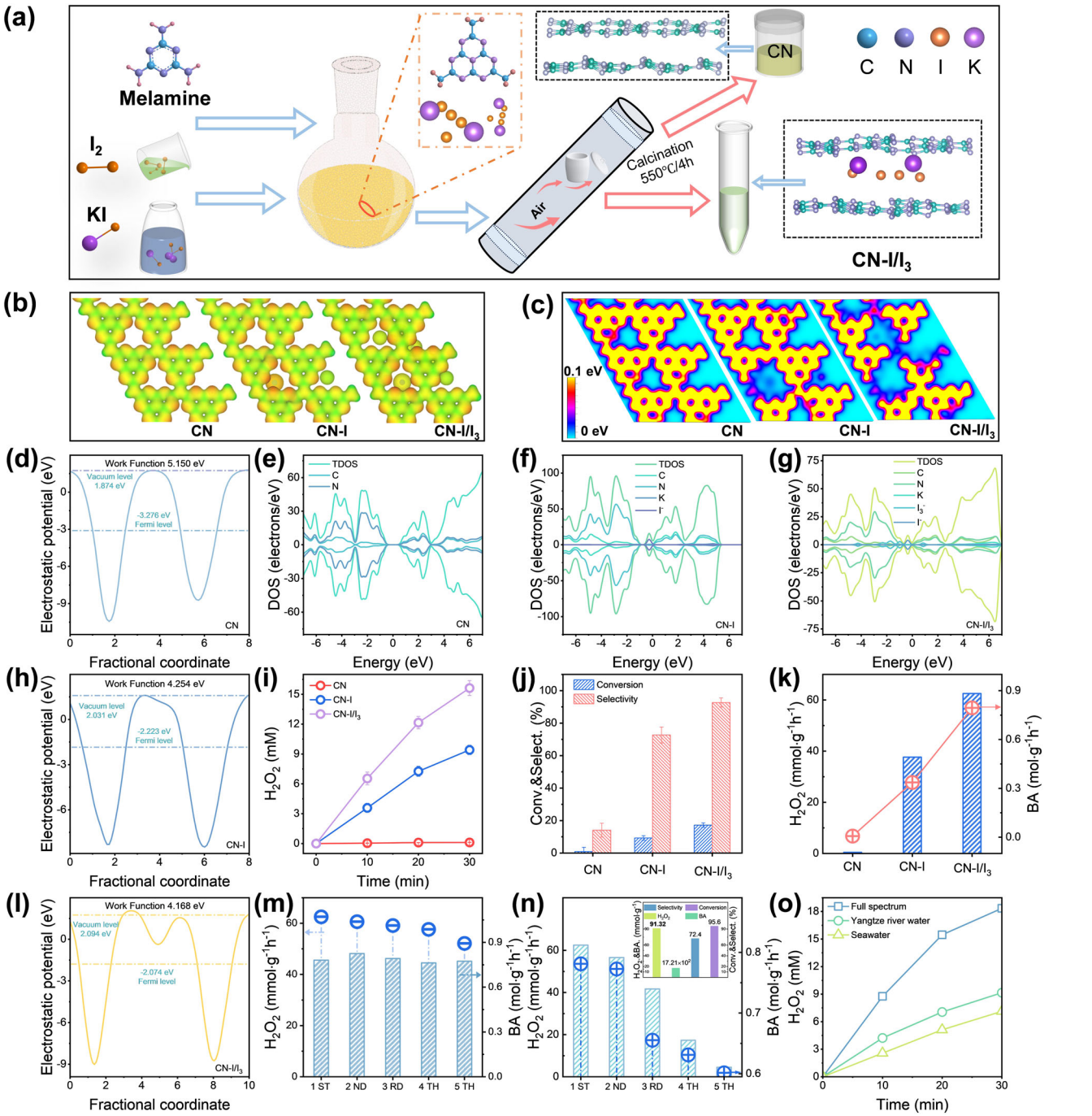

Fig. 1 | Theoretical prediction and activity validation of targeted catalysts. **a** Schematic synthesis of CN and CN-I/I_3. **b**, **c**, **d**, **e**, **f**, **g**, **h**, **I** electrostatic potential (**b**) two-dimensional electron density (**c**), surface work function (**d**, **h**, **I**), and electronic state density (**e**, **f**, **g**) of CN, CN-I, and CN-I/I_3. **i**, **j**, **k** The H_2O_2 production (**i**), BzOH conversion rate, benzaldehyde selectivity (**j**), and corresponding evolution rates (**k**) for CN, CN-I, and CN-I/I_3. The error bars represent the standard deviation of three replicate tests. **m**, **n**, **o** The stability evaluation of CN-I/I_3 (**m**), the sustained recycling performance of BzOH, Inset: Corresponding yield and selectivity (**n**), and H_2O_2 production performance, (**o**) in different reaction solutions.

alcohol (BzOH) was used as the organic substrate to evaluate the performance of a precisely engineered catalyst. This assessment was conducted within an optimized reaction system using the six-flux model (Fig. 1i and Supplementary Figs. 5–7). Incorporating KI into the catalyst notably amplified its capacity for H_2O_2 production. Furthermore, the subsequent addition of I_2 to the CN-I framework resulted in a discernible secondary enhancement in H_2O_2 by CN-I production. Compared to the baseline CN and the CN-I variant, CN co-polymerized with both KI and I_2 (CN-I/I_3) demonstrated a stronger photocatalytic activity, achieving an apparent quantum yield of 34.61% at 400 nm. This performance largely surpassed similar reported systems for the artificial photosynthesis of H_2O_2 (Supplementary Fig. 8). The catalytic activity for H_2O_2 decomposition was not notably inhibited (Supplementary Fig. 9), suggesting that the observed improvement was likely attributable to the enhanced crystallinity and the formation of I^-/I_3^- redox mediators within its layered structure. To optimize the yield of photocatalytically produced H_2O_2, a strategy involving segmented addition of the organic substrate was implemented during the reaction process (Supplementary Figs. 11–15). This approach increased H_2O_2 yield from 12.34 mM to 15.63 mM, indicative of more efficient

https://doi.org/10.1038/s41467-024-52158-z

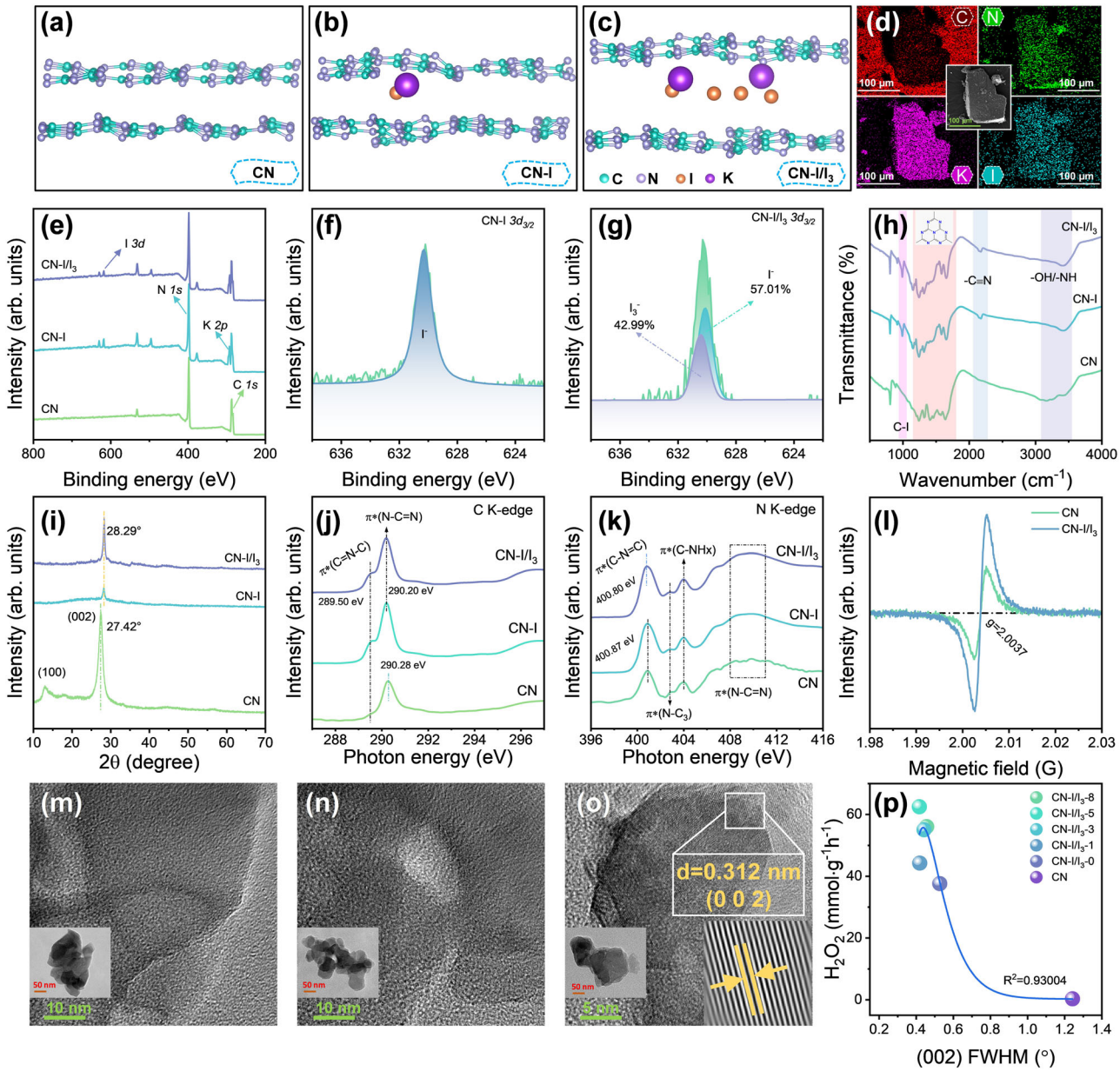

Fig. 2 | Qualitative and quantitative characterizations. a, **b**, **c** Optimized CN (**a**), CN-I (**b**), and CN-I/I_3 (**c**) geometric structures with an isosurface value of 0.009 e/Bohr^3. **d** TEM-EDS mappings of CN-I/I_3. **e**–**k** XPS spectra (**e**, **f**, **g**), FT-IR spectra (**h**), XRD patterns (**i**), C K-edge (**j**), and N K-edge (**k**) XANES spectra of CN, CN-I, and CN-I/I_3. **l** ESR spectra of CN and CN-I/I_3. **m**, **n**, **o** TEM (inset), and HR-TEM images of CN (**m**), CN-I (**n**), and CN-I/I_3 (**o**). **p** Relationship between H_2O_2 production and FWHM value of the (002) plane for samples with different CN-I-I_2 ratios.

utilization of photo-generated carriers. The successful H_2O_2 production using various organic substrates corroborates the effectiveness of this enhanced photocatalytic strategy.

In this study, the efficacy of H_2O_2 photo-production and concurrent oxidation for benzaldehyde (BA) synthesis was meticulously investigated (Fig. 1j, k; Supplementary Figs. 16 and 17). Copolymerization with both KI and KI/I_2 markedly improved H_2O_2 production. Significantly, the CN-I/I_3 sample exhibited exceptional performance in H_2O_2 generation, reaching 62.52 mmol g^{-1} h^{-1}, which was approximately 143.0 times higher than that of pristine CN (0.436 mmol g^{-1} h^{-1}), and displayed optimal BzOH oxidation efficiency. The conversion rate of BzOH using CN-I/I_3 w was around 17.18%, with a high BA selectivity of 92.65%, in stark contrast to the 0.94% conversion rate and 14.06% selectivity observed with unmodified CN.

Interestingly, an analysis of the functional relationship between photocatalytic rates of H_2O_2 and BA across different samples revealed high correlation coefficients, up to 0.970 (Supplementary Fig. 19). This strong correlation underscores a synergistic effect between photocatalytic reduction and oxidation processes, enabling dual-efficient production H_2O_2 and BA while fully utilizing generated electrons and holes. Additionally, the specifically engineered CN-I/I_3 system demonstrated effective production of H_2O_2, 2,5-diformylfuran (a selective oxidation product of hydroxymethylfurfural, achieving 82.59% selectivity), and dihydroxyacetone (a selective oxidation product of glycerol, with 74.88% selectivity). This result was achieved even when using diverse reactants such as 5-hydroxymethylfurfural and glycerol. These results highlight the system's prominent adaptability in coupling the selective oxidation of organic substrates with the photoproduction of H_2O_2 (Supplementary Fig. 21 and Supplementary Table 3). After five cycles of reuse, CN-I/I_3 retained its photocatalytic activity with minimal change (Fig. 1m). In the fifth cycle, H_2O_2 yield remained above 50 mmol g^{-1} h^{-1}, and BA yield reached 0.77 mol g^{-1} h^{-1},

indicating its excellent durability in both H_2O_2 generation and selective BzOH oxidation. In various complex environments, including different pH values and the presence of assorted ionic species, CN-I/I_3 consistently achieved high H_2O_2 yields (Supplementary Fig. 22). It also maintained significant activity in continuous H_2O_2 production without alterations in its structural and chemical properties, as evidenced by Scanning electron microscopy (SEM), X-ray diffraction spectroscopy (XRD), X-ray photoelectron spectroscopy (XPS), and Fourier-transform infrared spectroscopy (FT-IR) analyses after repeated reaction cycles (Supplementary Figs. 23–25), further confirming its stability and resistance to interference.

Notably, cyclic utilization of BzOH increased the conversion rate from 17.18% to 95.60% after five reactions, accompanied by significantly enhanced yields of H_2O_2 (91.32 mmol g^{-1}) and BA (1.72 mol g^{-1}) (Fig. 1n), suggesting a higher potential for practical application. The effectiveness of the catalyst was further validated by substantial H_2O_2 production in real-world samples, including Yangtze River water (9.16 mM) and Yellow Sea seawater (7.13 mM) (Fig. 1o), highlighting its applicability.

Physicochemical characterizations of target catalysts

To verify the successful synthesis of the required catalyst, a comprehensive chemical structure analysis of the prepared catalysts was performed using XPS, X-ray absorption near-edge structure spectroscopy (XANES), FT-IR, and XRD (Fig. 2e–k; Supplementary Figs. 26–36, and Supplementary Tables 4–7). Deconvolution of high-resolution XPS spectra for *C 1 s* and *N 1 s* revealed characteristic peaks at ~284.8, 286.0, 288.0, 398.0, 399.0, and 400.0 eV, corresponding to C=C, C-NH_x/C, N-C=N, C-N=C, N-C_3, and C-N-H functionalities within the CN framework[30] (Supplementary Figs. 28, 29, 32,33). These XPS findings, along with their fitting analyses, suggest that the co-polymerization with KI or KI/I_2 successfully integrated K and I elements into the CN framework without altering its inherent chemical structure. The *K 2p* and *I* $3d_{3/2}$ spectra of CN-I and CN-I/I_3 showed subtle shifts near 293.0/295.0 and 630.0 eV, respectively, compared to standard KI, affirming the incorporation of K and I into the CN lattice rather than existing as mere KI aggregates. Notably, in the *I* $3d_{3/2}$ spectrum of CN-I/I_3, a new peak indicative of I_3^- emerged, contrasting with the CN/KI spectrum. This observation suggested that the addition of I_2 resulted in the formation of I_3^- ($KI + I_2 \rightarrow KI_3$), potentially acting as a redox mediator alongside I^-, thereby enhancing the transport of photo-generated charge carriers during the photocatalytic process.

The electronic environments of C and N in CN, CN-I, and CN-I/I_3 were then examined using XANES (Fig. 2j, k). The C-K-edge XANES spectra of these samples exhibited characteristic resonances around 290.0 eV, corresponding to π*(N-C=N) transitions. In CN-I and CN-I/I_3, these π*(N-C=N) transition peaks were negatively shifted by approximately 0.08 eV compared to pristine CN, a shift attributable to the increased electron density around carbon atoms following co-polymerization with KI and KI/KI_3. Additionally, a distinct shoulder peak at 289.5 eV in CN-I and CN-I/I_3, absent in CN, was observed, indicative of enhanced in-plane and interlayer interactions in these modified samples. The N-K-edge XANES spectra revealed similar electron transition peaks among all samples, including π*(C-N=C), π*(N-C_3), π*(C-NH_x), and π*(N-C=N). The only notable difference was the upward shift of the π*(C-N=C) transition peak in CN-I/I_3 by about 0.07 eV compared to CN and CN-I, suggesting that I_3^- incorporation increased π* electron density, thereby providing additional electrons for reduction reactions.

The XRD analyses of CN revealed characteristic diffraction peaks at 12.9° (100) and 27.7° (002), corresponding to the in-plane stacking and interfacial packing of heptazine units, respectively[31]. The KI or KI/I_2 co-polymerization altered the crystal structure, leading to the disappearance or weakening of certain lattice plane diffraction peaks. The persistence of the (002) peak indicated the retention of heptazine units, while the absence of the (100) peak and a slight shift of the (002) peak towards higher angles suggested reduced interlayer spacing and a denser structure, generally indicative of enhanced crystallinity[32,33].

Compared to CN and CN-I, CN-I/I_3 exhibited smaller average pore sizes and increased thickness, confirming the denseness of their structures (Supplementary Fig. 39). As anticipated, high-resolution transmission electron microscopy (HR-TEM) images of CN-I/I_3 showed lattice stripes corresponding to the (002) plane, with the quantity and quality of these stripes increasing with the amount of I_2 co-polymerized (Fig. 2o and Supplementary Fig. 40). In contrast, the HR-TEM results of CN and CN-I lacked lattice fringes (Fig. 2m, n), suggesting that the mixed salt (KI/KI_3) in KI/I_2 might enhance crystallinity by facilitating in-plane 'sewing' and interlayer 'cutting' of CN[34]. The slight transition of CN-I/I_3 to a more crystalline PHI phase further substantiated this perspective[35–37] (Supplementary Fig. 38).

A functional relationship was established between the full width at half maximum (FWHM) value of the (002) plane, and the photocatalytic H_2O_2 production rate (Fig. 2p). A significant negative correlation between the FWHM value and H_2O_2 production underscored the critical role of enhanced crystallinity in improving the photocatalytic activity of CN-I/I_3. This enhancement was further attributed to the potential formation of I^-/I_3^- redox mediators induced by KI/I_2 co-polymerization and the associated increase in unpaired electron density in CN-I/I_3 compared to CN (Fig. 2l), facilitating more efficient separation of photo-generated charge carriers.

Therefore, the qualitative characterization results affirmatively suggest the improved crystallinity of CN-I/I_3 and the potential formation of the I^-/I_3^- redox mediators. Furthermore, the observed configurations aligned with DFT predictions corroborated the precise synthesis of the catalyst.

Electronic structure and carrier separation properties

Optical properties are pivotal in assessing the catalytic performance of photocatalysts. To this end, UV–visible diffuse reflectance spectroscopy (UV–Vis DRS), Tauc plot analysis, and Mott-Schottky (MS) assessment were utilized to investigate the effects of KI or KI/I_2 co-polymerization on the electronic and optical attributes of the photocatalyst (Fig. 3a and Supplementary Figs. 41–43). Compared to CN, both CN-I and CN-I/I_3 displayed a slight red shift in optical absorption spectra and a reduction in band gap width. This shift indicates that co-polymerization with KI or KI/I_2 enhances the light-harvesting efficiency of the photocatalyst. Subsequent band edge position analyses revealed that this co-polymerization effectively modulated the conduction band (CB) position. The addition of I_2 to CN-I/I_3 resulted in a downward shift of its CB position, likely linked to increased crystallinity[38]. The modified CB positions (≤−0.73 eV) were strategically aligned above the reduction potentials of both single-electron ($O_2 + e^- \rightarrow {}^{\cdot}O_2^-$ + e^- + $2H^+ \rightarrow H_2O_2$, $E_{NHE} = -0.33$ eV) and double-electron pathways ($O_2 + 2H^+ + 2e^- \rightarrow H_2O_2$, $E_{NHE} = 0.68$ eV) in the ORR process. This indicates that the co-polymerization of KI or KI/I_2, while facilitating the necessary reduction potential for efficient H_2O_2 generation, simultaneously maximized the valence band (VB) position, enhancing the oxidative capacity for selective oxidation of organic substrates. Also, by augmenting the H^+ supply, the H_2O_2 production could be simultaneously improved.

Beyond band structure modifications, the co-polymerization of KI or KI/I_2 was anticipated to influence the separation of photo-generated carriers. CN exhibited a broad and intense photoluminescence (PL) emission peak centered around 450 nm (Fig. 3b). Conversely, CN-I and CN-I/I_3 markedly reduced PL intensities, with CN-I/I_3 exhibiting almost negligible emission. Time-resolved PL spectra were employed to analyze the charge separation process and the average lifetimes of photo-generated charge carriers. The average lifetimes for CN, CN-I, and CN-I/I_3 were 3.84 ns, 0.95 ns, and 0.9 ns, respectively. The substantial

https://doi.org/10.1038/s41467-024-52158-z

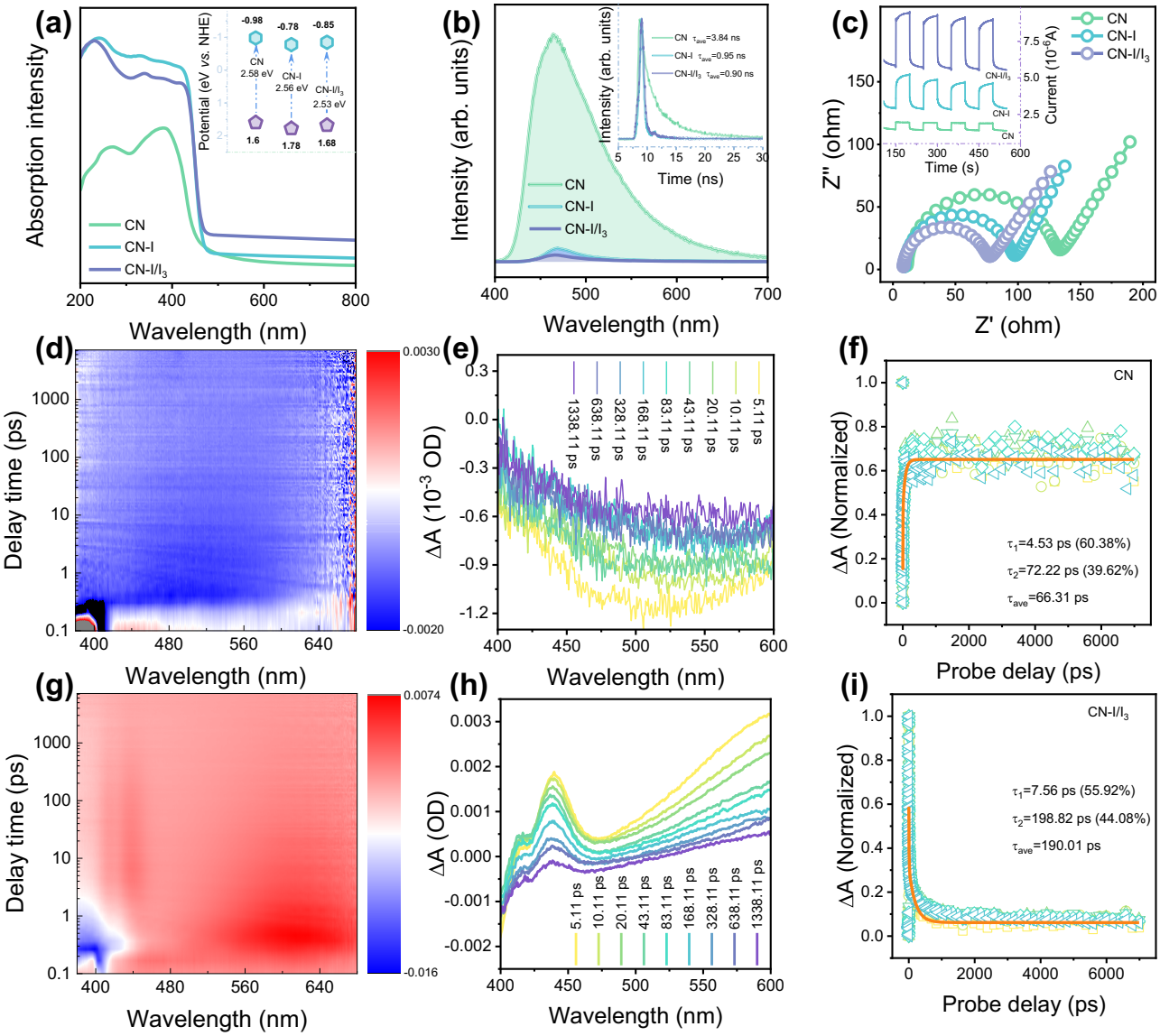

Fig. 3 | Investigation of optical properties and carrier transfer kinetics. **a**, **b**, **c** UV–Vis DRS spectra, Inset: The corresponding band structure diagram (**a**), PL spectra, Inset: TR-PL spectra (**b**), and EIS spectra, Inset: photocurrent response (**c**) of CN, CN-I, and CN-I/I_3. **d**, **e**, **f**, **g**, **h**, **i** Three-dimensional contour plots of *fs*-TAS (**d**, **g**), transient absorption kinetics at 375 nm within 1400 ps (**e**, **h**), and transient absorption intensity decay curves (**f**, **i**) within the 500–550 nm range for CN-I and CN-I/I_3.

decrease in PL emission peaks and shorter carrier lifetimes in CN-I and CN-I/I_3 suggest accelerated separation of electron-hole pairs. CN-I/I_3, in particular, exhibited the fastest carrier separation rate, likely due to its significantly enhanced crystallinity and the formation of I^-/I_3^- redox mediators. Additionally, CN-I/I_3 exhibited the highest photocurrent response, the greatest open-circuit potential difference, the smallest electrochemical impedance spectroscopy (EIS) arc radius, and the most rapid electron accumulation (Fig. 3c and Supplementary Figs. 44–47). These findings collectively demonstrate its stronger efficiency in transferring photo-generated charge carriers compared to both CN and CN-I.

To delineate the decay kinetics of photo-generated charge carriers, femtosecond transient absorption spectroscopy (*fs*-TAS) was utilized to probe the absorption characteristics of intermediate species. This analysis was aimed at shedding light on the impacts of augmented crystallinity and the introduction of I^-/I_3^- redox mediators on the oxidation and reduction reactions occurring on the photocatalyst's surface. Upon 375 nm excitation, the 3D contour plots and absorption profiles of CN and CN-I/I_3 were delineated in Fig. 3d, g. The negative absorption features observed in CN are indicative of ground-state bleaching or stimulated emission (SE), while CN-I/I_3 displayed a pronounced positive absorption feature in the excited-state absorption (ESA) spectrum, implying effective retention of photo-generated electrons, holes, or electron-hole pairs[39,40]. Representative dynamic decay traces captured by *fs*-TAS are presented in Fig. 3f, i, and the kinetic curves for CN and CN-I/I_3 in the 500–550 nm wavelength range were accurately modeled using bi-exponential functions. The derived time constants, $\tau 1$ and $\tau 2$ are representative of photo-generated electron-hole pair recombination and shallow electron trapping processes, respectively[41,42]. Compared to CN ($\tau 1 = 4.53$ ps, $\tau 2 = 72.22$ ps), CN-I/I_3 ($\tau 1 = 7.56$ ps, $\tau 2 = 198.82$ ps) exhibited prolonged durations for both photo-generated electron-hole recombination and shallow electron trapping.

The observed retardation in the decay of photo-generated carriers and the amplified shallow electron trapping in CN-I/I_3 suggest an increased likelihood and abundance of active electron transfers during photocatalysis. This facilitates the persistence of a substantial number

https://doi.org/10.1038/s41467-024-52158-z

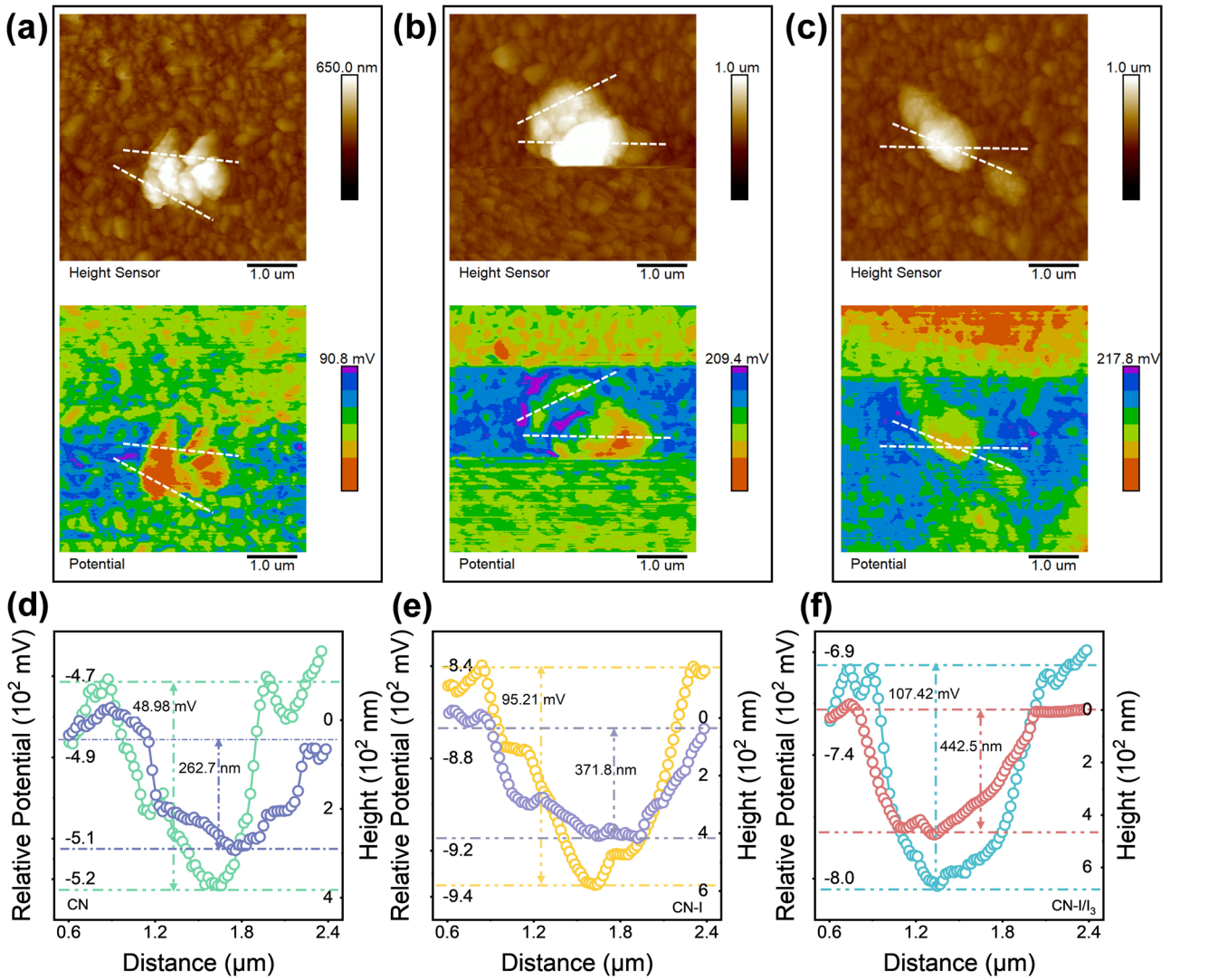

Fig. 4 | In-depth evaluation of charge transfer potential. a, **b**, **c**, **d**, **e**, **f** Surface morphology, height difference distribution, and surface potential difference distribution under illumination for CN (**a**, **d**), CN-I (**b**, **e**), and CN-I/I_3 (**c**, **f**).

of active electrons and holes, thereby enhancing the efficiency of H_2O_2 generation and the selective conversion of organic substrates.

To corroborate the separation process of photo-generated carriers on the catalyst surface, Kelvin probe force microscopy (KPFM) was implemented to visualize the surface potential with a nanoscale spatial resolution (Fig. 4). The contact potential difference (CPD) was assessed based on the potential differential between the Kelvin probe tip and the sample. Under illumination, the surface potentials of CN, CN-I, and CN-I/I_3 shifted negatively, a phenomenon attributed to interlayer charging owing to the segregation of photo-generated charge carriers[43]. The CPDs of CN, CN-I, and CN-I/I_3 progressively increased to 48.98 mV, 95.21 mV, and 107.42 mV, respectively, under light exposure (Fig. 4d–f). The most pronounced ΔCPD signal in CN-I/I_3 indicates an accelerated separation of photo-generated electron-hole pairs, facilitated by the newly formed I^-/I_3^- redox mediators and improved crystallinity.

Overall, under the combined influences of an internally generated electric field due to heightened crystallinity and the I^-/I_3^- redox mediators, CN-I/I_3 exhibited an enhanced capability for light absorption and prolonged participation of carriers in the reaction process, compared to CN and CN-I. These empirical observations are congruent with the increased yields of H_2O_2 and BA demonstrated by CN-I/I_3.

Synergistic photocatalytic reduction and oxidation reactions

To elucidate the fundamental mechanism of H_2O_2 production, a series of experiments were conducted under varying atmospheric conditions and through active species trapping (Fig. 5a). The marked contrast in H_2O_2 yields under N_2 and O_2 atmospheres irrefutably confirmed the essential role of O_2 as a reactant in H_2O_2 synthesis. The complete inhibition of H_2O_2 photo-production under $K_2Cr_2O_7$ shielding, coupled with a progressive decline in free charge intensity in the presence of TEMPO as an electron scavenger, decisively indicated the crucial involvement of photo-generated electrons in H_2O_2 formation (Fig. 5c). Notably, the negligible H_2O_2 yield in the presence of p-benzoquinone (pBQ) underscored the pivotal role of superoxide radicals ($^{\cdot}O_2^-$) as intermediates in the production process. Electron paramagnetic resonance (EPR) experiments using 5,5-dimethyl-1-pyrroline N-oxide (DMPO) as a spin trap and nitroblue tetrazolium (NBT) as a detection probe further corroborated the presence of $^{\cdot}O_2^-$ (Fig. 5b and Supplementary Figs. 48–50). Compared to CN, the more pronounced $^{\cdot}O_2^-$ EPR signal and greater NBT reduction observed with CN-I/I_3, suggested a more efficient H_2O_2 generation in CN-I/I_3. These findings robustly support the hypothesis that a two-step single-electron reduction pathway of O_2 ($O_2 \rightarrow {}^{\cdot}O_2^- \rightarrow H_2O_2$) was the predominant mechanism for H_2O_2 generation.

https://doi.org/10.1038/s41467-024-52158-z

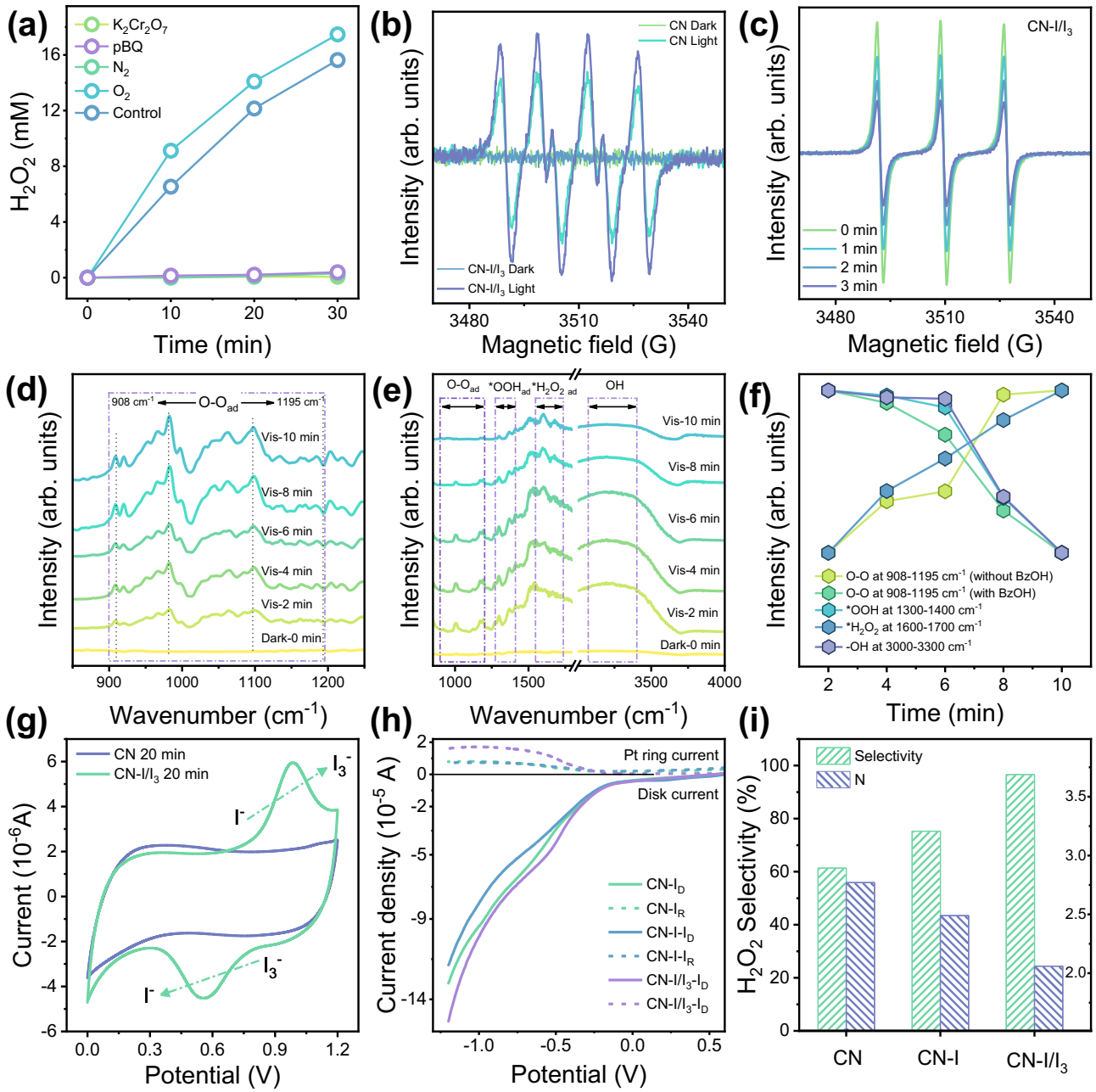

Fig. 5 | Synergistic mechanism for photocatalytic reduction and oxidation reactions. a Photocatalytic H_2O_2 production using CN-I/I_3 with different reaction gases, electron capture agent ($K_2Cr_2O_7$), and $^{\cdot}O_2^-$ scavenger (p-BQ). **b** EPR signals of superoxide radicals for CN and CN-I/I_3. **c** EPR signals of free charges for CN-I/I_3. **d**, **e**, **f** In situ FT-IR spectra of CN-I/I_3 under different reaction conditions and corresponding peak intensity changes with the light irradiation time. **g** Quasi-in situ cyclic voltammetry curves of CN and CN-I/I_3. **h**, **i** Polarization curves (**h**), corresponding H_2O_2 selectivity, and average electron transfer number (**i**) for CN, CN-I, and CN-I/I_3.

In situ diffuse reflectance infrared Fourier-transform spectroscopy (in situ DRIFTS) was utilized to further delineate the mechanistic details of H_2O_2 production and BzOH oxidation under various testing conditions (Supplementary Fig. 51). The in situ FT-IR spectra of CN-I/I_3 in both dry and BzOH aqueous solutions, as shown in Fig. 5d, e, revealed distinctive vibrational bands in the ranges of 908–1156 cm^{-1}, 1300–1400 cm^{-1}, 1600–1700 cm^{-1}, and 3000–3300 cm^{-1}. These bands were attributed to adsorbed O_2, *OOH, *H_2O_2, and -OH groups (originating from the BzOH solution) on CN-I/I_3, respectively[44,45]. In a dry environment, the increasing intensity of adsorbed O_2 peaks over time indicated effective O_2 adsorption by CN-I/I_3. Conversely, in the BzOH aqueous solution, a decrease in these characteristic peaks with time was observed (Fig. 5f), suggesting that in the presence of a proton source, CN-I/I_3 efficiently activates adsorbed O_2 for H_2O_2 production. The rise in vibrational signals corresponding to *OOH and *H_2O_2 with prolonged exposure in the BzOH solution provided direct evidence of H_2O_2 formation. Additionally, the diminishing vibrational signal of hydroxyl (-OH) groups from BzOH over time confirmed the oxidative dehydrogenation of BzOH. The observed increase in the *H_2O_2 signal and decrease in the -OH signal indicated the concurrent occurrence of photocatalytic reduction (ORR) and oxidation (BzOH oxidation) processes. These concurrent reactions mutually facilitated each other by synchronously consuming photo-generated electrons and holes, efficiently utilizing photo-generated charge carriers.

In quasi-in situ cyclic voltammetry (CV) experiments, the electrochemical active surface area (ECSA) of CN-I/I_3 demonstrated a

progressive increase with the reaction time, in contrast to pristine CN. Such an increase, coupled with the emergence of distinct oxidation ($I^- \rightarrow I_3^-$) and reduction ($I_3^- \rightarrow I^-$) peaks, provided solid evidence for the formation of an I^-/I_3^- redox mediator within the catalyst structure[46] (Fig. 5g and Supplementary Fig. 54). The parallel trends in ECSA enhancement and oxidation-reduction peak profiles observed in CN-I and CN-I/I_3 during the reaction indicated their mutual engagement in converting the I^-/I_3^- redox mediator. However, CN-I/I_3 displayed a notably larger ECSA both pre- and post-reaction compared to CN-I and exhibited more pronounced changes in the oxidation-reduction peaks at equivalent reaction durations. This large disparity suggests that the incorporation of I_2 effectively pre-implanted the I^-/I_3^- redox mediator within the catalyst. The pre-formation of the redox mediator facilitated more rapid oxidation-reduction cycling in the photocatalytic process, accelerating the transfer of photo-generated charge carriers and enhancing overall photocatalytic activity.

The rotating ring-disk electrode (RRDE) technique was further employed to evaluate the selectivity of O_2 reduction and determine the number of electron transfers (*N*) during the ORR, based on the recorded reduction and oxidation currents (Fig. 5h, i and Supplementary Fig. 55). The estimated N values for CN, CN-I, and CN-I/I_3 were 2.77, 2.49, and 2.06, respectively. Notably, the electron transfer characteristics of CN-I/I_3 closely aligned with a $2e^-$ O_2 reduction process, favoring the selective production of H_2O_2 with a high selectivity of 96.62%[47]. This result suggests the enhanced suitability of CN-I/I_3 for targeted H_2O_2 generation, positioning it as a potent candidate for selective photocatalytic applications.

Thorough dissection of dual-channel high-value conversion mechanisms

The pivotal contribution of KI or KI/KI_3 co-crystallization to the enhancement of photocatalytic activity was further elucidated through DFT calculations. Electronic density differences for CN-I and CN-I/I_3 are depicted in Fig. 6a, b and Supplementary Fig. 56, with regions of electron increase and decrease represented by green and yellow, respectively. In CN-I, charge transfer predominantly occurred from I^- to the CN framework. In contrast, CN-I/I_3 exhibited more extensive charge redistribution due to concurrent charge transfer from the CN framework to both I^- and I_3^-. These multiple charge transfer pathways augmented the electron exchange efficiency of CN-I/I_3 and substantiated the existence of the I^-/I_3^- redox shuttle mediator. The electron density distributions of the lowest unoccupied molecular orbitals (LUMO) and highest occupied molecular orbitals (HOMO), along with LUMO+1 and HOMO-1, for CN, CN-I, and CN-I/I_3, provided detailed insights into their charge transfer characteristics (Supplementary Fig. 57). In CN, HOMOs were predominantly located on N atoms, while LUMOs were concentrated on C atoms. This uniform distribution led to efficient charge carrier recombination in CN[48]. The incorporation of I^- facilitated aggregation of HOMOs, creating an uneven spatial distribution of HOMOs and LUMOs. The insertion of I_3^- intensified these spatial charge distribution disparities, effectively reducing e^--h^+ pairs recombination and enhancing charge separation, thus favoring photocatalytic reactions.

Moreover, the Gibbs free energy changes in the ORR and BzOH oxidation processes intricately demonstrated the efficacy of KI/KI_3 co-polymerization (Fig. 6d–g). The intercalation of I^- or I^-/I_3^- led to uneven charge redistribution, enhancing O_2 adsorption via van der Waals interactions between the material's fixed dipole and the induced dipole of O_2 molecules. Specifically, the free energies for O_2 adsorption on CN, CN-I, and CN-I/I_3 were calculated to be +0.074 eV, +0.044 eV, and +0.03 eV, respectively, with corresponding O-O bond lengths post-adsorption of 1.24 Å, 1.26 Å, and 1.27 Å (Fig. 6h and Supplementary Fig. 58). Lower adsorption energies and longer O-O bond lengths implied the increased affinity for O_2 adsorption and activation on CN-I/I_3. Due to the synergistic effect of I^- and I_3^-, the ORR pathway on CN-I/I_3 exhibited a more favorable energy profile compared to CN and CN-I, facilitating the formation of the critical intermediate *OOH and its subsequent hydrogenation to H_2O_2. The concurrent selective oxidation of BzOH to BA was also analyzed. Following BzOH adsorption, the α-H atom was first removed, then the -O-H atom, leading to benzaldehyde formation. The thermodynamically rate-determining step involved the removal of the α-H atom. Notably, CN-I/I_3 displayed a more pronounced uneven charge distribution, resulting in a longer C-H bond length in adsorbed BzOH (1.104 Å) compared to CN (1.099 Å) and CN-I (1.101 Å). This disparity significantly lowered the energy barrier for the rate-determining step ($*C_7H_8O \rightarrow *C_7H_7O$). Furthermore, CN-I/$I_3$-BzOH exhibited stronger electron transfer tendencies from BzOH to the material compared to CN-BzOH and CN-I-BzOH (Fig. 6c and Supplementary Fig. 59), indicating more pronounced charge accumulation at the adsorption site of benzyl alcohol, which facilitated charge transfer to the material, consuming more holes during the oxidation process. In summary, due to the incorporation of I^-/I_3^- and enhanced crystallinity, both the ORR and BzOH oxidation pathways on CN-I/I_3 were energetically more favorable than on CN and CN-I, significantly promoting the synergistic production of H_2O_2 and BA.

Based on these findings, a likely mechanism for the dual-channel photosynthesis using CN-I/I_3^- was proposed (Fig. 6i). The I^-/I_3^- redox shuttle mediator played a crucial role in speeding up charge separation and ensuring a continuous carriers supply. This mechanism allowed the photo-generated electrons to quickly interact with adsorbed O_2 through a two-step, single-electron pathway, converting O_2 into $^{\bullet}O_2^-$ and subsequently into H_2O_2. Concurrently, the holes participated in the selective oxidation of BzOH, effectively producing BA and yielding excess protons for ORR.

Does the substantial accumulation of H_2O_2 have a practical application potential?

Leveraging its enhanced crystalline structure and the synergistic interaction of I^-/I_3^- redox mediators, the CN-I/I_3 exhibited exceptional photocatalytic performance, with its H_2O_2 yield largely surpassing those of other recently reported photocatalysts under analogous conditions (Fig. 7a, Supplementary Fig. 60 and Supplementary Tables 8–9). The photocatalytic efficacy of CN-I/I_3 was further evaluated under natural sunlight. In various environments, including deionized water (H_2O_2, 158.48 mM, 1.58 mmol; BA, 2.55 mmol), authentic Yangtze River water (H_2O_2, 81.25 mM, 0.81 mmol; BA, 2.80 mmol), and Yellow Sea seawater (H_2O_2, 71.01 mM, 0.71 mmol; BA, 3.31 mmol), CN-I/I_3 efficiently generated H_2O_2 and selectively produced BA over 8 h of natural sunlight exposure (Fig. 7b and Supplementary Fig. 61a). In an expanded reactor setup with a 100 mL working volume, CN-I/I_3 consistently achieved a high H_2O_2 yield (33.16 mM).

For practical applications, the used CN-I/I_3 could be readily recovered through techniques such as centrifugation and filtration. However, implementing a continuous flow system with CN-I/I_3 immobilized on a membrane (containing 5 mg CN-I/I_3) simplifies this process. This system demonstrated a high H_2O_2 yield of 1.82 mmol under 8 h of natural sunlight at a flow rate of 0.8 mL min^{-1}, underscoring the potential for solar panel-level H_2O_2 photosynthesis using CN-based photocatalysts (Fig. 7c and Supplementary Fig. 61d).

To better align with practical industrial development, we developed an integrated process system for the photocatalytic production, concentration, and separation of products (Supplementary Fig. 63). By loading the photocatalyst onto hydrophobic melamine foam, we further eliminated the need for solid-liquid separation while establishing a gas-liquid-solid catalytic interface to enhance mass transfer rates, further promoting the co-production of BA and H_2O_2. In a natural light photocatalytic production trial lasting up to 21 h (12 h on the first day, 9 h on the second), the conversion efficiency of BzOH reached 94.99%, with a BA yield of 6.29 mmol. The produced H_2O_2 and BA mixture could be easily concentrated through low-temperature (50 °C)

https://doi.org/10.1038/s41467-024-52158-z

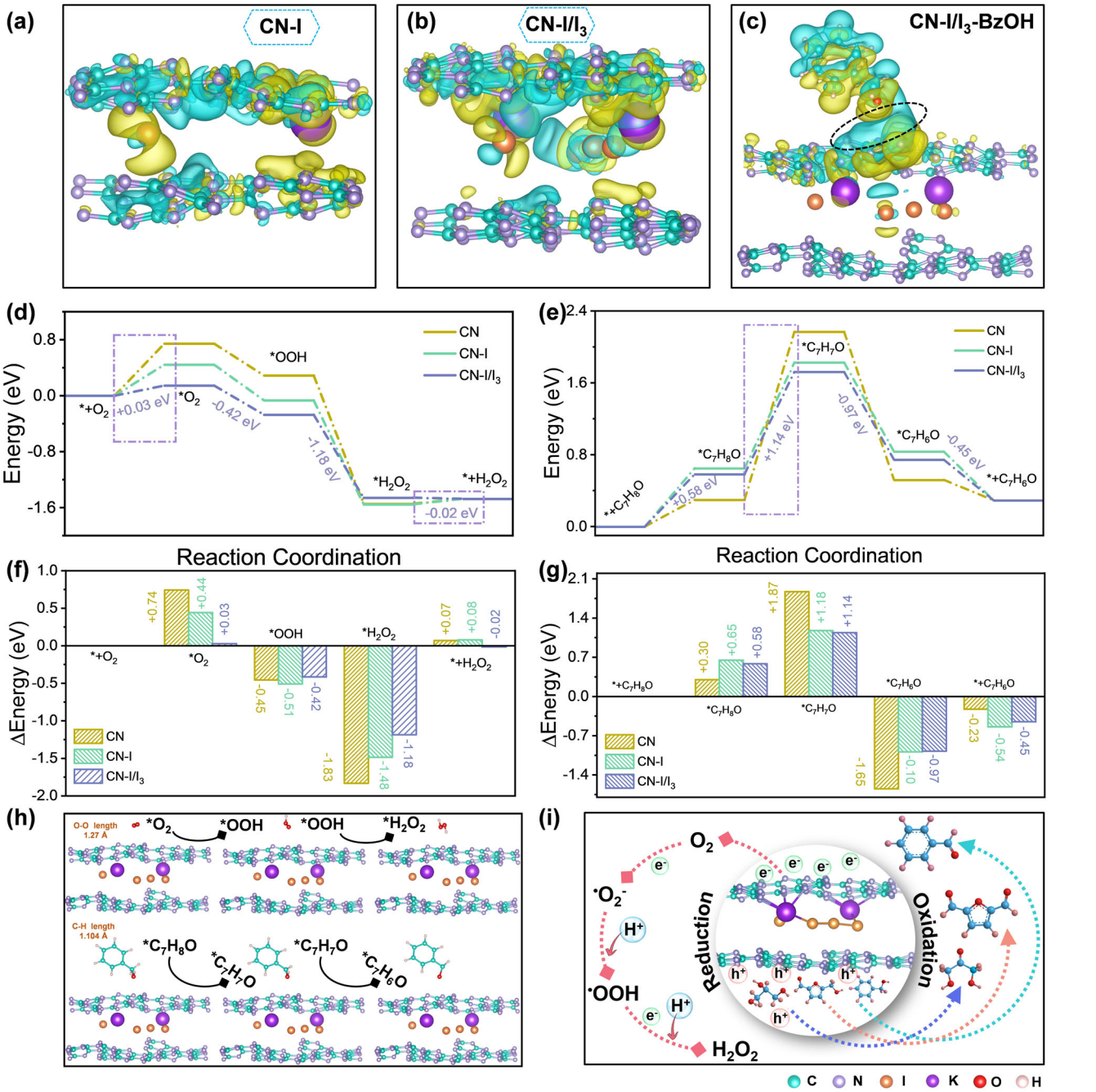

Fig. 6 | DFT assists in revealing the intrinsic mechanism. a, **b**, **c** Electron density difference diagrams of CN-I (**a**), CN-I/I_3 (**b**), and CN-I/I_3-BzOH (**c**) with an isosurface value of 0.009 e/Bohr^3 (Regions of electron increase and decrease represented by green and yellow, respectively). **d**, **f** Energy diagrams of H_2O_2 evolution reaction on CN, CN-I, and CN-I/I_3. **e**, **g** Energy diagrams of BzOH oxidation reaction on CN, CN-I, and CN-I/I_3. **h** Adsorption structures of *O_2, *OOH, *H_2O_2, *C_7H_8O, *C_7H_7O, *C_7H_6O on CN-I/I_3. **i** Schematic diagrams of the enhanced oxidation and reduction conversions.

evaporation. In the first concentration process, the H_2O_2 concentration increased from 47.28 mM to 97.39 mM, and in the second concentration process, it increased from 254 mM to 496.67 mM, achieving a yield of 10.93 mmol. Due to the difference in phase properties, the concentrated mixture solution was separated using a simply hydrophobically modified stainless steel mesh. The higher-density BA flowed out from beneath the hydrophobic membrane, while the H_2O_2 aqueous solution remained above it (Supplementary Fig. 62). The successful implementation of this integrated process system provided a promising feasibility for the practical application of photocatalytic simultaneous production of two high-value chemicals.

Also, CN-I/I_3's dual enhancement mechanism was highly effective in water purification, activating periodate (PI) under natural sunlight. The system achieved complete decolorization of 100 mg/L rhodamine B (RhB) within 14 min (Supplementary Fig. 65) and complete degradation of 20 mg/L sulfamethoxazole (SMX) in 6 min (Fig. 7f). The treated water exhibited a higher density of *E. coli* survival, healthier wheat growth, and normal development of zebrafish embryos, accompanied by a reduction in the toxicity of the intermediates. These results indicate that the CN-I/I_3-PI system possesses strong purification and detoxification capabilities for organics-contaminated water after activation under natural sunlight (Supplementary Figs. 66–70).

https://doi.org/10.1038/s41467-024-52158-z

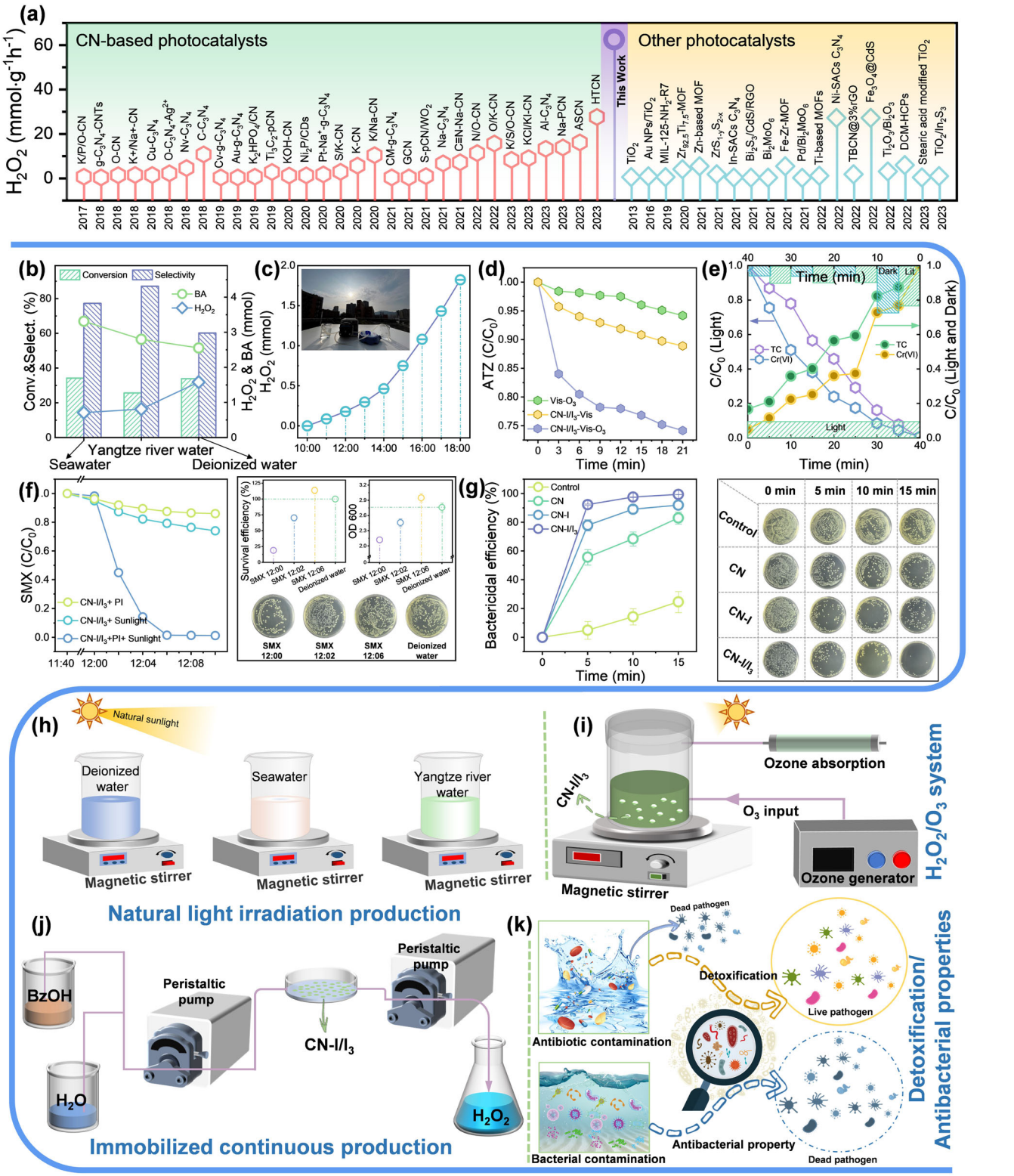

Fig. 7 | Multi-dimensional and intensive application assessment. a Comparison with other recently reported photocatalysts for the production of H_2O_2. **b** CN-I/I_3 under natural light irradiation: H_2O_2 production, BzOH conversion, and benzaldehyde selectivity in different solutions. **c** H_2O_2 production by continuous immobilization of CN-I/I_3 under natural light, Inset: Continuous production of H_2O_2 physical diagrams. **d** Removal of ATZ in H_2O_2/O_3 combined system. **e** Removal of TC-Cr(VI) by CN-I/I_3 under intermittent light irradiation. **f** Efficiency of CN-I/I_3 sample in activating PI for SMX removal under natural light, and OD600 values and bacterial counts of *E. coli*/cells in solution at different time intervals. **g** Comparison of disinfection effects using different samples on *E.* coli/cells and corresponding bacterial counts of *E. coli*. The error bars represent the standard deviation of three replicate tests. **h**, **i**, **j**, **k** Scenario diagrams for the applications of CN-I/I_3 system.

The efficiently accumulated H_2O_2 in CN-I/I_3 could be effectively utilized for in situ applications. The H_2O_2 generated by CN-I/I_3 was harnessed for *E. coli* disinfection, exhibiting outstanding antibacterial efficacy. Specifically, CN-I/I_3 achieved an impressive 99.38 ± 0.04% inactivation rate of *E. coli* within 15 min of exposure to visible light irradiation (Fig. 7g), demonstrating significant potential for practical applications in medical and health-related fields. Additionally, in the H_2O_2/O_3 system, the combined treatment process significantly outperformed the individual processes in degrading atrazine, illustrating a prominent synergistic effect (Fig. 7d).

Considering the well-documented memory photocatalytic effect associated with CN-based materials, the post-irradiation catalytic activity of CN-I/I_3 was assessed for the removal of tetracycline and hexavalent chromium (TC-Cr(VI)) (Fig. 7e and Supplementary Fig. 71a). After 40-min continuous illumination, TC-Cr(VI) was completely removed, a process attributed to the oxidative breakdown of TC-Cr(VI) bonds and the oxidation of TC by photo-generated holes. The reduction of Cr(VI) was presumably driven by photo-generated electrons. Interestingly, under intermittent light irradiation, nearly equivalent TC-Cr(VI) removal to that achieved with continuous 40-min exposure was accomplished in 20 min. The substantial removal of both TC and Cr(VI) during dark periods suggests the release of electrons even in the absence of light, underscoring the material's effective utilization of stored energy.

Therefore, the well-designed CN-I/I_3, under both natural and visible light irradiation, has demonstrated prominent potential in simulated environmental and antibacterial scenarios. These findings position CN-I/I_3 as a promising and yet relatively unexplored photocatalyst with broad application prospects.

Discussion

Inspired by the commonplace phenomenon of KI decomposition and underpinned by comprehensive theoretical calculations, this study leveraged I_2 to synthesize a KI/KI_3 mixed salt, facilitating the formation of a highly *semi*-crystalline CN embedded with an I^-/I_3^- redox mediators (CN-I/I_3) by a secondary calcination process. The integration of theoretical simulations and extensive experimental characterizations revealed that the heightened crystallinity and stability were instrumental in enhancing the built-in electric field. In concert with the embedded I^-/I_3^- redox mediators, this effect significantly improved the dissociation of photo-generated carriers. This dual-action design efficiently maximized the utilization of photo-generated electrons and holes, thus producing both high values of H_2O_2 and BA in a coupled photocatalytic system. Further empirical validation underscored the versatile potential of CN-I/I_3 in various applications. Notably, CN-I/I_3 exhibited an impressive H_2O_2 production of 158.48 mM (1.58 mol) under natural sunlight. This efficiency could be augmented through integrating with photothermal effects to boost catalytic performance.

Furthermore, CN-I/I_3 could effectively activate oxidant for the purification and regeneration of contaminated wastewater, demonstrating capabilities in *E. coli* cultivation and disinfection, and highlighting its potential in combating resistant bacteria. This suggests that CN-I/I_3 could be particularly effective in applications involving antibiotic-resistant genes, especially in treating medical wastewater. The potential of CN-I/I_3 extended to the photocatalytic eradication of tumor cells, adding to its multifaceted utility. Interestingly, CN-I/I_3 retained significant catalytic activity in dark conditions post-light exposure, hinting at potential applications in alternating light-dark reactions, which may be relevant in bio-inspired designs. Crucially, the synergistic effect observed in the industrialized H_2O_2/O_3 system underscores the strong practical applicability of CN-I/I_3. These findings position CN-I/I_3 as a highly competitive yet underexplored photocatalyst in the market. This research contributes substantially to the understanding and harnessing of electrons and holes in redox reactions, aiming to orchestrate a notable advance in this field. The above results indicate that accurately engineered CN- or other semiconductor-based photocatalysts can facilitate high-value, concurrent production at both the oxidation and reduction ends of the spectrum.

Methods

Chemicals and reagents

Melamine (MA, AR), potassium iodide (KI, AR/GR), iodine (I_2), potassium titanium oxalate ($C_4H_2K_2O_{10}Ti$, AR), sulfuric acid (H_2SO_4), sodium hydroxide (NaOH), triethylamine, isopropyl alcohol (IPA, AR), methanol (MeOH, AR), ethanol (EtOH, AR), ethylene glycol, *tert*-butanol (TBA, AR), sulfamethoxazole (SMX), rhodamine B, p-benzoquinone (pBQ, AR), silver sulfate (Ag_2SO_4, AR), potassium dichromate ($K_2Cr_2O_7$, AR), sodium chloride (NaCl), potassium chloride (KCl), magnesium chloride ($MgCl_2$), potassium sulfate (K_2SO_4), sodium nitrate ($NaNO_3$), sodium carbonate (Na_2CO_3), and potassium hydrogen phosphate (K_2HPO_4) were all purchased from Sinopharm Chemical Reagent Co., China, Sigma-Aldrich Chemical Reagent Co., China, Macklin Chemical Reagent Co., China, or Shanghai Chemical Reagent Co., China. The Yangtze River water was collected from Chongqing City, China, while the seawater was collected from the Yellow Sea, China. All solutions were prepared with Milli-Q water with an 18.25 MΩ/cm resistivity.

Synthesis of photocatalysts.

(a) **CN preparation:** A homogeneous mixture of 10 g of melamine was placed in a covered alumina crucible and subjected to a calcination process within a tube furnace under an air atmosphere. This process was carried out for 4 h, employing a controlled heating rate of 2.5 °C/min. After the calcination, the resultant product was meticulously ground, thoroughly washed, and then efficiently separated and collected through centrifugation.

(b) **CN-I preparation:** A mixture consisting of 1 g of CN and varying amounts of KI—specifically, 1 g, 2 g, and 3 g—was prepared in 80 mL of deionized water. This mixture was subjected to ultrasonic treatment for 10 min to ensure homogeneity. Subsequently, it was heated to 80 °C in an oil bath, with continuous stirring to facilitate solvent evaporation and to aid in product collection. The resultant material was then transferred to a covered alumina crucible for calcination. This calcination process was conducted in a tube furnace under an air atmosphere for 4 h, maintaining a steady heating rate of 2.5 °C/min.

After calcination, the product was thoroughly ground, washed, and then efficiently separated using centrifugation. The different samples were systematically named based on the weight of KI used in their preparation, resulting in CN-I-1, CN-I-2 (collectively referred to as CN-I), and CN-I-3.

(c) **CN-I/I_3 preparation:** Typically, 1 g of CN, 2 g of KI, and varying amounts of I_2—specifically, 1 mg, 3 mg, 5 mg, and 8 mg—were added to 80 mL of deionized water. This mixture was subjected to ultrasonication for 10 min to ensure homogeneity, followed by heating at 80 °C in an oil bath. Continuous stirring was employed during this heating process to facilitate solvent evaporation and the collection of the resultant product. The gathered product was subsequently placed in a covered alumina crucible and calcinated within a tube furnace under an air atmosphere. This calcination was conducted over 4 h, with a controlled heating rate of 2.5 °C/min. Post-calcination, the obtained material was meticulously ground, washed, and separated via centrifugation. The different samples, differentiated by the weight of I_2 used, were sequentially named CN-I/I_3-1, CN-I/I_3-3, CN-I/I_3-5 (collectively as CN-I/I_3), and CN-I/I_3-8.

Dual-channel evaluation of H_2O_2 production and BzOH oxidation

The coupled photocatalytic reaction involving oxygen reduction and selective alcohol oxidation was conducted in a 100 mL double-layered glass reactor. Initially, 5 mg of the photocatalyst was ultrasonically dispersed in 10 mL of an aqueous BzOH solution for 5 min to ensure

uniform distribution. This was followed by a dark stirring for 10 min to establish adsorption-desorption equilibrium. The catalytic reaction was then initiated using a 300 W xenon lamp (PLS-FX300HU, Beijing Perfectlight Technology Co., China, $\lambda \geq 420$ nm) as the light source, maintaining a constant ambient temperature of 25 °C. During the reaction, aliquots of 1 mL were sampled at 10-min intervals. The photocatalyst was subsequently separated from these samples through filtration using a 0.22 μm membrane filter. The H_2O_2 concentration in the sampled aliquots was quantified employing the potassium titanium oxalate method. Post-reaction, the solution was centrifuged, and the concentrations of BzOH and BA were analyzed using high-performance liquid chromatography (HPLC). The conversion rate of BzOH and selectivity of BA were calculated according to the Eqs. 1 and 2:

$$\text{Conversion}\,(\%) = \left[(C_0 - C_{BzOH})/C_0\right] \times 100\% \quad (1)$$

$$\text{Selectivity}\,(\%) = [C_{BA}/(C_0 - C_{BzOH})] \times 100\% \quad (2)$$

where C_0 is the original concentration of BzOH, C_{BzOH} is the concentration of the residual BzOH, and C_{BA} is the concentration of the corresponding BA after the photocatalytic reaction.

Characterizations

Near-edge X-ray absorption fine structure spectroscopy (EXAFS) analysis was conducted at the BL12B beamline of the Hefei National Synchrotron Radiation Laboratory. Kelvin probe force microscopy (KPFM) measurements were performed using a conductive probe (SCM-PIT-V2) on an Atomic Force Microscope (AFM, Bruker Multimode 8). In situ infrared spectroscopy was conducted on a spectrometer (INVENIO S, Bruker Co., Germany, equipped with a high-temperature reaction chamber and liquid nitrogen-cooled MCT). Additionally, in situ infrared spectroscopy was performed again at the synchrotron source. Ultrafast transient absorption spectroscopy (*fs*-TAS) analysis was carried out using the Helios pump-probe detection system (Ultrafast Systems LLC) and an amplified femtosecond laser system (Coherent). Quasi-in situ CV tests were conducted using a standard three-electrode system with pure water as the electrolyte on a CHI660E electrochemical workstation. The crystallographic phases of the synthesized samples were characterized using a Bruker D8 Advanced X-ray diffractometer (XRD), employing Cu Kα X-ray radiation at operational settings of 40 kV and 40 mA. The microstructural attributes of the various samples were meticulously examined utilizing a field emission scanning electron microscope (FESEM, Apreo 2 C, Thermo Fisher Inc., USA) and a transmission electron microscope (TEM) equipped with FEI Tecnai G20 (Hitachi Co., Japan). Elemental analyses and mapping results were conducted using energy-dispersive X-ray spectroscopy (EDS) on a JSM-7900F spectrometer. Optical properties, including light absorption profiles, were analyzed using ultraviolet-visible diffuse reflectance spectroscopy (UV–Vis DRS) on a UV3600-plus spectrometer, covering a spectral range of 250–800 nm. X-ray photoelectron spectroscopy (XPS) measurements for detailed chemical state and elemental composition analysis were performed using an ESCALAB 250Xi spectrometer (Thermo Fisher Inc., USA). Surface area determinations were carried out using the Brunauer-Emmett-Teller (BET) method, utilizing a Builder 4200 instrument (Tristar II 3020 M, Micromeritics Co., USA). The identification of surface functional groups present in the samples was conducted through Fourier-Transform Infrared Spectroscopy (FT-IR, Nicolet Is10, Thermo Fisher Inc., USA). Photoluminescence (PL) characteristics and time-resolved PL spectra were obtained using an FLS-1000 fluorescence spectrometer. To identify the active species present in the photocatalytic system, electron spin resonance (ESR) spectroscopy (ER200-SRC, Bruker Co., USA) was used, utilizing 2,2,6,6-tetramethylpiperidine-N-oxyl (TEMPO) and 5,5-dimethylpyrroline N-oxide (DMPO) as spin-trapping reagents. Furthermore, the acute and chronic toxicological impacts of sulfamethoxazole (SMX, antibiotics) and its degradation products were evaluated using the ecological structure-activity relationships (ECOSAR) and toxicity estimation software tool (T.E.S.T) systems. This assessment provides crucial insights into the environmental and health-related implications of SMX and its derivatives.

Analysis of optical properties of the photocatalysts. A comprehensive understanding of a photocatalyst's optical properties is imperative for the identification and development of high-performance photocatalysts. The optical characteristics of a catalyst are fundamental in determining its photon absorption efficiency and, by extension, its photocatalytic performance[49]. Building upon the foundations of existing research, the current study employed a six-flux model to evaluate the light absorption capacity of the photocatalyst[50,51]. It is noteworthy that the six-flux model facilitates the calculation of critical optical parameters such as the total photon absorption rate (TRPA), local volume rate of photon absorption (LVRPA), and apparent optical thickness (τ_{app}). These parameters are instrumental in enabling a detailed and comprehensive assessment of the photocatalyst's efficiency.

At present, LVRPA is recognized as a critical metric for quantifying the local photon absorption within the reaction medium[52]. Accurately calculating the synthesized catalyst's optical thickness, as delineated through Eqs. 3–7, is an essential step in determining the LVRPA.

$$\kappa^* = \frac{\int_{\lambda\,\min}^{\lambda\,\max} \kappa_\lambda^* \mathrm{I}_\lambda d\lambda}{\int_{\lambda\,\min}^{\lambda\,\max} \mathrm{I}_\lambda d\lambda} \quad (3)$$

$$\sigma^* = \frac{\int_{\lambda\,\min}^{\lambda\,\max} \sigma_\lambda^* \mathrm{I}_\lambda d\lambda}{\int_{\lambda\,\min}^{\lambda\,\max} \mathrm{I}_\lambda d\lambda} \quad (4)$$

$$\tau = (\sigma^* + \kappa^*) C_{cat} L \quad (5)$$

$$\beta^* = \sigma^* + \kappa^* \quad (6)$$

where C_{cat} is the photocatalyst loading, σ^* and κ^* are the spectral average specific scattering and absorption coefficients, respectively, and L is the characteristic length of light extinction in the reactor, which is 80 mm. Obtained scattering coefficient (σ^*), absorption coefficient (κ^*), and extinction coefficient (β^*) are listed in Supplementary Table 1.

The optical thickness of different materials could be calculated as follows:

$$\tau_{app} = a\tau\sqrt{1 - \omega_{corr}^2} \quad (7)$$

The determination of the local volume rate of photon absorption (LVRPA) for the catalyst was conducted using Eqs. 8–13, as shown in Supplementary Table 2. Notably, a positive correlation was observed between the concentration of the catalysts and their respective optical thicknesses. As the concentration of the catalysts increased, there was a corresponding linear enhancement in the LVRPA at the catalyst surface, as depicted in Supplementary Fig. 2. Significantly, among the evaluated catalysts, CN-I/I_3 demonstrated the steepest slope in this relationship. This finding underscores its superior optical properties, aligning well with the predictions made by theoretical calculations.

Furthermore, considering factors such as the optimal optical thickness range of the comprehensive reactor (1.8-4.4), mass transfer rate, etc., a catalyst concentration of 0.5 g/L was chosen for the

photocatalytic activity evaluation.

$$LVRPA = \frac{I_0 \tau_{app}}{\omega_{corr}(1-\gamma)L}\left[(\omega_{corr} - 1 + \sqrt{1-\omega_{corr}^2})e^{-\frac{x\tau_{app}}{L}} + \gamma(\omega_{corr} - 1 - \sqrt{1-\omega_{corr}^2})e^{\frac{x\tau_{app}}{L}}\right] \quad (8)$$

Among a, b, ω_{corr}, and γ are defined below:

$$a = 1 - \omega p_f - \frac{4\omega^2 p_s^2}{1 - \omega p_f - \omega p_b - 2\omega p_s} \quad (9)$$

$$b = \omega p_b + \frac{4\omega^2 p_s^2}{1 - \omega p_f - \omega p_b - 2\omega p_s} \quad (10)$$

$$\omega_{corr} = b/a \quad (11)$$

$$\gamma = \frac{1 - \sqrt{1-\omega_{corr}^2}}{1 + \sqrt{1-\omega_{corr}^2}} e^{-2\tau_{app}} \quad (12)$$

$$TRPA = \int_0^L LVRPA.dx \quad (13)$$

Degradation of sulfamethoxazole (SMX). The direct degradation of SMX was carried out in a 100 mL double-layer glass beaker. In brief, 5 mg of CN-I/I_3 was ultrasonically dispersed in 50 mL of SMX solution. The mixture was stirred in the dark for an additional 10 min to ensure adsorption-desorption equilibrium. Photocatalytic reactions were initiated by adding 1 mM sodium periodate (PI, $NaIO_4$) under natural light exposure. At 2-min intervals, 1 mL of the solution was collected, and the concentration of SMX was determined using HPLC (1260 Infinity, Agilent Inc., USA). To further assess the detoxification capability of CN-I/I_3 under natural light exposure, LB culture media with varying reaction times were prepared. These media were used to inoculate *Escherichia coli* (*E. coli*), and their OD600 values were monitored, along with the colony survival rate on agar plates.

Zebrafish cultivation for real toxicity assessment. Initially, a trio of zebrafish—one female and two males—were placed in a tank filled with a nutrient-rich solution, where they were cultured for a duration of 12 h. This was done with the aim of obtaining a substantial quantity of zebrafish embryos. Following this initial phase, the first batch of collected embryos was subjected to a washing process using deionized water. The purpose of this step was to meticulously remove any surface impurities present in the embryos. Eight-cell stage embryos were then selected under a microscope for further use. To investigate the detoxification performance of CN-I/I_3 activated PI on SMX-contaminated water under natural sunlight, solutions obtained from reactions in the CN-I/I_3-PI-Sunlight and CN-I/I_3-sunlight systems were designated as experimental groups. Solutions containing only SMX and the nutrient solution (NC) served as control groups. These solutions were collectively referred to as exposure solutions. The selected zebrafish embryos were placed in a cell culture plate, then 1 mL of nutrient solution and 1 mL of exposure solution were added to each well. Each exposure solution was cultured five times. The development of embryos in each group was observed and recorded under a microscope every 24 h until hatching was completed in the NC group. Realistic toxicity assessment using zebrafish cultivation presented above can better reveal the response system's processing performance and subsequent utility.

Cultivation or disinfection of *E. coli*. Inoculate 50 μL of *E. coli* (BL21, wild bacteria) freeze-dried powder into prepared LB culture medium and cultivate in a shaking incubator at 37 °C (180 rpm, Honour, HNY-200B) for 10 h to obtain activated strains. In the in situ antibacterial experiment, sterilized catalyst and benzyl alcohol were simultaneously added to a 20 mL quartz test tube containing activated strains. The investigation was conducted under the irradiation of a 300 W xenon lamp ($\lambda \geq 420$ nm). Suspension was collected every 5 min, diluted 10,000 times with PBS solution, and spread on agar plates. The plates were then incubated at 37 °C for 18 h, and the colony count on the agar plates was calculated.

The procedure for *E. coli* culture was the same as above, except the LB culture medium was prepared with SMX solution of different reaction times. Before spreading on agar plates, the dilution factor was 100,000. The antibacterial efficiency calculation formula is as follows (Eq. 14):

$$Ar = (M - N)/M \times 100\% \quad (14)$$

where M refers to the initial number of colonies and N represents the number of colonies after photocatalytic sterilization. All experiments were carried out on a clean workbench (AIRTECH, SW-CJ-1FD). All the consumables used in the experiments were sterilized at 121 °C for 15 min in an autoclave (IMJ-85A, STIK Co., USA) or under UV radiation (254 nm) for 20 min.

Performance assessment of the H_2O_2/O_3 degradation system. Performance evaluation of atrazine (ATZ, pesticide residues) degradation was carried out under natural light conditions employing the combined H_2O_2/O_3 system. Specifically, a mixture comprising 10 mg of the catalyst and a trace amount of BzOH was ultrasonically dispersed in an aqueous solution containing ATZ. During the experiment, O_3 was continuously introduced into the solution under natural light irradiation. Samples of 1 mL volume were systematically collected at 3-min intervals for analysis. The concentration of ATZ in these samples was subsequently quantified using high-performance liquid chromatography (HPLC, 1260 Infinity, Agilent Inc., USA). This methodological approach allowed for a precise and systematic evaluation of the catalyst's efficacy in degrading ATZ in an environmentally relevant photocatalytic system.

The future development of an integrated system for H_2O_2 production, encompassing in situ utilization, concentration, collection, and reuse, holds substantial potential for practical applications. Such a system would not only streamline the production process of H_2O_2 but also optimize its use, thereby enhancing overall efficiency and sustainability. This integrated approach is auspicious for industries where H_2O_2 is a crucial reactant or cleaning agent, offering a more environmentally friendly and cost-effective solution.

Photoelectrochemical measurements. The obtained catalyst was electrochemically characterized using a standard three-electrode system on a CHI 760E electrochemical workstation (Shanghai Chenhua Instrument Co., China). The characterization included electrochemical impedance spectroscopy (EIS), transient photocurrent (i-t) curves, and Mott-Schottky (MS) curves. The reference electrode and counter electrode were Ag/AgCl and Pt plate electrodes, respectively. The working electrode was an FTO glass coated with the catalyst, prepared from 5 mg of the catalyst, 2 mL of ethanol, and 20 μL of Nafion solution. The electrolyte used was 0.1 M Na_2SO_4.

The rotating ring-disk electrode (RRDE) test was conducted in a three-electrode reaction cell to describe the oxygen reduction reaction characteristics of the obtained catalyst. The reference electrode and counter electrode were Ag/AgCl and Pt plate electrodes, respectively. The working electrode consisted of an RRDE composed of a glassy carbon disk and a platinum ring. The prepared slurry mentioned above (6 μL) was coated onto the glassy carbon disk and vacuum-dried to prepare the working electrode.

The H_2O_2 production selectivity is calculated according to Eq. 15:

$$H_2O_2(\%) = \frac{2 \times i_R}{N \times |i_D| + i_R} \times 100 \quad (15)$$

The electron transfer number (n) is calculated according to Eq. 16:

$$n = \frac{4|i_D|}{|i_D| + \frac{i_R}{N}} \quad (16)$$

where i_R and i_D are the ring and disk currents, respectively, and N is the collection efficiency of the RRDE ($N = 0.25$).

Details of apparent quantum yield (AQY) test. The AQY for artificial H_2O_2 synthesis in the CN-I/I_3 system was measured using a 400 ± 15 nm band-pass filter. The calculation formula is provided in Eq. 17.

$$\begin{aligned} AQY &= \frac{\text{number of reacted electrons}}{\text{number of incidented electrons}} \times 100\% \\ &= \frac{2nN_A}{\frac{SPt}{hc/\lambda}} \times 100\% = \frac{2nN_A hc}{SPt\lambda} \times 100\% \end{aligned} \quad (17)$$

where n is the amount of H_2O_2 molecules (mol, 46.15×10^{-6} mol), N_A is the Avogadro constant (6.022×10^{23}/mol), h is the Planck constant (6.626×10^{-34} JS), c is the speed of light (3×10^8 m/s), S is the irradiation area (m^2, 15.89×10^{-4} m^2), P is the intensity of irradiation light (W m^{-2}, 27.9 W m^{-2}), t is the photoreaction time (s, 1800 s), λ is the wavelength of the monochromatic light (m, 400×10^{-9} m). Combining the above data, the AQY at 400 nm of our system was calculated to be 34.61%.

Quasi-in situ UV–Vis absorption spectroscopy test. To systematically evaluate the stability of the optimized catalytic system, quasi-in situ UV–Vis absorption spectroscopy was employed for real-time detection of potentially leached I_3^-. The photocatalytic reaction followed the same procedure as artificial H_2O_2 synthesis but without benzyl alcohol. Samples were taken at specific intervals and centrifuged, and the supernatant was collected for full-spectrum scanning on a UV–Vis spectrophotometer (TU1391901) within a wavelength range of 200–500 nm.

Catalyst immobilization procedure. The catalyst immobilization setup was similar to the working electrode preparation method described in Photoelectrochemical measurements, with the distinction that the prepared slurry was sprayed onto a 2 cm diameter circular filter membrane, achieving a loading amount of 5 mg.

Quantification of $^{\bullet}O_2^-$. The generation of $^{\bullet}O_2^-$ during the photocatalytic reaction was detected using nitroblue tetrazolium (NBT) as a probe. Specifically, 9.5 μM of NBT and 5 mg of the photocatalyst were added to 10 mL of benzyl alcohol aqueous solution. The mixture was ultrasonicated and allowed to react in the dark for 10 min to establish adsorption-desorption equilibrium. Upon initiating the light source, samples were collected at specific intervals, and centrifuged, and the supernatant's absorbance was measured at 259 nm using a UV–Vis spectrophotometer. The yield of $^{\bullet}O_2^-$ was calculated based on the stoichiometric ratio of the reaction between $^{\bullet}O_2^-$ and NBT (4: 1).

Hydrophobic stainless steel mesh membrane modification procedure. Cut stainless steel mesh (400 mesh) was ultrasonically cleaned with acetone and deionized water for 20 min to remove dust and stains. Polydimethylsiloxane (PDMS, 2 g) was added to hexane (40 mL) and stirred thoroughly for 30 min, followed by the addition of silica nanoparticles (1 g) and continued stirring for another 30 min. Subsequently, silicone resin (0.2 g) was added as a curing agent. The prepared mixture was sprayed onto the stainless steel mesh from a distance of 30 cm using a spray gun at a pressure of 275 kPa. The mesh was then dried in an oven at 60 °C for 5 h to solidify. The unmodified stainless steel mesh is referred to as SS, while the modified version is named MSS.

Hydroponic experiment of wheat seeds. Hydroponic experiments with wheat seeds were conducted using water samples purified by different catalytic systems, alongside original SMX and deionized water, to evaluate the detoxification effects of various catalytic systems on contaminated water from a botanical perspective. Specifically, 20 healthy, plump wheat seeds were selected and placed in culture dishes equipped with filter paper at the bottom, to which 10 mL of different water sources were added. The growth of the seeds was recorded at set intervals, with water sources replenished as needed. After 7-d cultivation, all the wheat seedlings were collected, and differences in root length and shoot length among each group were recorded.

Details of theoretical calculations. We conducted density functional theory (DFT) calculations within the generalized gradient approximation (GGA) framework, employing the Perdew-Burke-Ernzerhof (PBE) formulation[53]. Brillouin zone of 2 × 2 × 1 k-points was applied for geometry optimization. Valence electrons were represented using a plane wave basis set with a kinetic energy cutoff of 400 eV. Partial occupancies of the Kohn–Sham orbitals were introduced using the Gaussian smearing method with a width of 0.05 eV. We ensured self-consistency in the electronic energy calculations, considering the energy change smaller than 10^{-5} eV as a convergence criterion. Moreover, geometry optimization was deemed convergent if the energy change was below 0.02 eV per Ångström (eV•$Å^{-1}$). To minimize artificial interactions between periodic images, we typically included a 15 Å thick vacuum layer at the surface. For the treatment of weak interactions, the DFT + D3 method was used, implementing Grimme's empirical correction scheme.

The photocatalytic production process of H_2O_2 can be represented by the following steps (Eqs. 18–21):

$$\textbf{Step 1 :} * + O_2 \rightarrow {}^*O_2 \quad (18)$$

$$\textbf{Step 2 :} {}^*O_2 + e^- + H^+ \rightarrow {}^*OOH \quad (19)$$

$$\textbf{Step3 :} {}^*OOH + e^- + H^+ \rightarrow {}^*H_2O_2 \quad (20)$$

$$\textbf{Step4 :} {}^*H_2O_2 \rightarrow * + H_2O_2 \quad (21)$$

The standard hydrogen electrode model was employed to calculate the free energy change (ΔG) of the ORR intermediate in the aforementioned reaction pathways[54,55]. $G(H^+)$ is typically described as $1/2\,G(H_2) - k_B T \ln(10) \times pH$ at non-zero pH ($p = 1$ bar, $T = 298.15\,K$). For each step, the reaction free energy was calculated by $\Delta G = \Delta E + \Delta ZPE - T\Delta S + \Delta G_U + \Delta G_{pH}$, where ΔE, ΔZPE, and $T\Delta S$ represent the total energy, zero-point energy, and entropy contribution obtained from DFT calculations, respectively. $\Delta G_U = -eU$, where e is the elementary charge, U is the electrode potential. ΔG_{pH} is the correction of H^+ free energy. The ΔG in H_2O_2 production can be calculated using the following formula (Eqs. 22–25).

$$\Delta G_1 = G(^*O_2) - G(O_2) - G(*) \quad (22)$$

$$\Delta G_2 = G(^*OOH) - G(^*O_2) + eU - 1/2G(H_2) + k_B T \ln(10) \times pH \quad (23)$$

$$\Delta G_3 = G(^*H_2O_2) - G(^*OOH) + eU - 1/2G(H_2) + kBT \ln(10) \times pH \quad (24)$$

$$\Delta G_4 = G(*) + G(H_2O_2) - G(*H_2O_2) \quad (25)$$

Reporting summary

Further information on research design is available in the Nature Portfolio Reporting Summary linked to this article.

Data availability

Data analyses are mainly carried out in the software Origin 2022 and XPS PEAK 41. The data that support the findings of this work are available within the manuscript, Supplementary information files, and Source Data File. Source data are provided in this paper. The X-ray crystallographic coordinates for structures (g-C_3N_4) reported in this study have been deposited at the Cambridge Crystallographic Data Centre (CCDC), under deposition numbers JCPDS 87-1526. Source data are provided in this paper.

References

1. Freese, T., Meijer, J. T., Feringa, B. L. & Beil, S. B. An organic perspective on photocatalytic production of hydrogen peroxide. *Nat. Catal.* **6**, 553–558 (2023).
2. Teng, Z. et al. Atomically dispersed antimony on carbon nitride for the artificial photosynthesis of hydrogen peroxide. *Nat. Catal.* **4**, 374–384 (2021).
3. Hou, H., Zeng, X. & Zhang, X. Production of hydrogen peroxide through photocatalytic processes: a critical review of recent advances. *Angew. Chem. Int. Edit.* **59**, 17356 (2019).
4. Liu, J. et al. Metal-free efficient photocatalyst for stable visible water splitting via a two-electron pathway. *Science* **347**, 970–974 (2015).
5. Li, Q. et al. Shear stress triggers ultrathin-nanosheet carbon nitride assembly for photocatalytic H_2O_2 production coupled with selective alcohol oxidation. *J. Am. Chem. Soc.* **145**, 20837–20848 (2023).
6. Wang, W. et al. Photothermal-enabled single-atom catalysts for high-efficiency hydrogen peroxide photosynthesis from natural seawater. *Nat. Commun.* **14**, 2493 (2023).
7. Dong, W. et al. Isomeric oligo (phenylenevinylene)-based covalent organic frameworks with different orientation of imine bonds and distinct photocatalytic activities. *Angew. Chem. Int. Edit.* **62**, e202216073 (2023).
8. Li, K. et al. H_2S involved photocatalytic system: a novel syngas production strategy by boosting the photoreduction of CO_2 while recovering hydrogen from the environmental toxicant. *Adv. Funct. Mater.* **32**, 2113002 (2022).
9. Yang, J., Jing, J. & Zhu, Y. A full-spectrum porphyrin-fullerene D-a supramolecular photocatalyst with giant built-in electric field for efficient hydrogen production. *Adv. Mater.* **33**, e2101026 (2021).
10. Luo, N. & Wang, F. Visible-light-driven co-production of diesel precursors and hydrogen from lignocellulose-derived methylfurans. *Nat. Energy* **258**, 575–584 (2019).
11. Wu, J., Wang, Y., Zhang, S., Liu, Y. & Wang, F. Poly (dibenzothiophene-S, S-dioxide)-Fe_2O_3 heterojunction for photocatalytic hydrogen production coupled with selective oxidation of benzyl alcohol. *Appl. Catal. B-Environ.* **332**, 122741 (2023).
12. Mennen, S. M. et al. The evolution of high-throughput experimentation in pharmaceutical development and perspectives on the future. *Org. Process. Res. Dev.* **23**, 1213–1242 (2019).
13. Shi, Y. et al. Homogeneity of supported single-atom active sites boosting the selective catalytic transformations. *Adv. Sci.* **9**, e2201520 (2022).
14. Zhao, W. et al. Accelerated synthesis and discovery of covalent organic framework photocatalysts for hydrogen peroxide production. *J. Am. Chem. Soc.* **144**, 9902–9909 (2022).
15. Wang, H., Yang, C., Chen, F., Zheng, G. & Han, Q. A crystalline partially fluorinated triazine covalent organic framework for efficient photosynthesis of hydrogen peroxide. *Angew. Chem. Int. Edit.* **61**, e202202328 (2022).
16. Cao, S., Low, J., Yu, J. & Jaroniec, M. Polymeric photocatalysts based on graphitic carbon nitride. *Adv. Mater.* **27**, 2150–2176 (2015).
17. Zhang, G. et al. Electron deficient monomers that optimize nucleation and enhance the photocatalytic redox activity of carbon nitrides. *Angew. Chem. Int. Edit.* **58**, 14950 (2019).
18. Liu, B. et al. Boosting O_2 reduction and H_2O dehydrogenation kinetics: surface N-hydroxymethylation of g-C_3N_4 photocatalysts for the efficient production of H_2O_2. *Adv. Funct. Mater.* **32**, 2111125 (2021).
19. Zhou, G. et al. Half-metallic carbon nitride nanosheets with micro grid mode resonance structure for efficient photocatalytic hydrogen evolution. *Nat. Commun.* **9**, 3366 (2018).
20. Yu, Z., Yue, X., Fan, J. & Xiang, Q. Crystalline intramolecular ternary carbon nitride homojunction for photocatalytic hydrogen evolution. *ACS Catal.* **12**, 6345–6358 (2022).
21. Algara-Siller, G. et al. Triazine-based graphitic carbon nitride: a two-dimensional semiconductor. *Angew. Chem. Int. Edit.* **53**, 7450–7455 (2014).
22. Zhang, J. et al. Improved charge separation in poly (heptazine-triazine) imides with semi-coherent interfaces for photocatalytic hydrogen evolution. *Angew. Chem. Int. Edit.* **61**, e202210849 (2022).
23. Zhang, G. et al. Optimizing optical absorption, exciton dissociation, and charge transfer of a polymeric carbon nitride with ultrahigh solar hydrogen production activity. *Angew. Chem. Int. Edit.* **56**, 13445–13449 (2017).
24. Li, F. et al. Understanding the unique S-scheme charge migration in triazine/heptazine crystalline carbon nitride homojunction. *Nat. Commun.* **14**, 3901 (2023).
25. Zhang, Y. et al. Molecular heptazine-triazine junction over carbon nitride frameworks for artificial photosynthesis of hydrogen peroxide. *Adv. Mater.* **35**, 2306831 (2023).
26. Liu, L.-L., Chen, F., Wu, J.-H., Chen, J.-J. & Yu, H.-Q. Synergy of crystallinity modulation and intercalation engineering in carbon nitride for boosted H_2O_2 photosynthesis. *Proc. Natl. Acad. Sci. USA* **120**, e2215305120 (2023).
27. Li, W. et al. Designing ternary hydrated eutectic electrolyte capable of four-electron conversion for advanced Zn-I_2 full batteries. *Energ. Environ. Sci.* **16**, 4502–4510 (2023).
28. Liu, X. et al. Integrating mixed halide perovskite photocatalytic hi splitting and electrocatalysis into a loop for efficient and robust pure water splitting. *Adv. Mater.* **35**, 2208915 (2023).
29. Chen, F. et al. Enhanced full solar spectrum photocatalysis by nitrogen-doped graphene quantum dots decorated BiO_{2-x} nanosheets: ultrafast charge transfer and molecular oxygen activation. *Appl. Catal. B-Environ.* **277**, 119218 (2020).
30. Fu, H. et al. Ultrathin porous carbon nitride bundles with an adjustable energy band structure toward simultaneous solar photocatalytic water splitting and selective phenylcarbinol oxidation. *Angew. Chem. Int. Edit.* **60**, 4951 (2021).
31. Xu, Y. et al. Homogeneous carbon/potassium-incorporation strategy for synthesizing red polymeric carbon nitride capable of near-infrared photocatalytic H_2 production. *Adv. Mater.* **33**, 2101455 (2021).
32. Zhang, G. et al. Ionothermal synthesis of triazine-heptazine-based copolymers with apparent quantum yields of 60% at 420 nm for solar hydrogen production from "Sea Water". *Angew. Chem. Int. Edit.* **130**, 9516–9520 (2018).
33. Ma, T. Single-crystal X-ray diffraction structures of covalent organic frameworks. *Science* **361**, 48–52 (2018).
34. Zhang, G. et al. In-plane charge transport dominates the overall charge separation and photocatalytic activity in crystalline carbon nitride. *ACS Catal.* **12**, 4648–4658 (2022).

35. Botari, T., Huhn, W., Lau, V. W.-h, Lotsch, B. V. & Blum, V. Thermodynamic equilibria in carbon nitride photocatalyst materials and conditions for the existence of graphitic carbon nitride g-C_3N_4. *Chem. Mater.* **29**, 4445–4453 (2017).
36. Kessler, F. K. et al. Functional carbon nitride materials-design strategies for electrochemical devices. *Nat. Rev. Mater.* **2**, 17030 (2017).
37. Wang, Y. et al. Current understanding and challenges of solar-driven hydrogen generation using polymeric photocatalysts. *Nat. Energy* **4**, 746–760 (2019).
38. Zhang, G. et al. Breaking the limitation of elevated coulomb interaction in crystalline carbon nitride for visible and near-infrared light photoactivity. *Adv. Sci.* **9**, e2201677 (2022).
39. Lin, H. et al. Molecular dipole-induced photoredox catalysis for hydrogen evolution over self-assembled naphthalimide nanoribbons. *Angew. Chem. Int. Edit.* **61**, e202117645 (2022).
40. Corp, K. L. & Schlenker, C. W. Ultrafast spectroscopy reveals electron-transfer cascade that improves hydrogen evolution with carbon nitride photocatalysts. *J. Am. Chem. Soc.* **139**, 7904–7912 (2017).
41. Xu, F. et al. Step-by-step mechanism insights into the TiO_2/Ce_2S_3 S-scheme photocatalyst for enhanced aniline production with water as a proton source. *ACS Catal.* **12**, 164–172 (2021).
42. Wang, W. et al. In situ protonated-phosphorus interstitial doping induces long-lived shallow charge trapping in porous C_3-N_4 photocatalysts for highly efficient H_2 generation. *Energy Environ. Sci.* **16**, 460–472 (2023).
43. Zhang, P. et al. Heteroatom dopants promote two-electron O_2 reduction for photocatalytic production of H_2O_2 on polymeric carbon nitride. *Angew. Chem. Int. Edit.* **132**, 16343–16351 (2020).
44. Luo, Y. et al. Sulfone-modified covalent organic frameworks enabling efficient photocatalytic hydrogen peroxide generation via one-step two-electron O_2 reduction. *Angew. Chem. Int. Edit.* **135**, e202305355 (2023).
45. Nayak, S., McPherson, I. J. & Vincent, K. A. Adsorbed intermediates in oxygen reduction on platinum nanoparticles observed by in situ IR spectroscopy. *Angew. Chem. Int. Edit.* **130**, 13037–13040 (2018).
46. Wang, X. et al. Double-photoelectrode redox desalination of seawater. *Water Res.* **239**, 120051 (2023).
47. Nosaka, Y. & Nosaka, A. Y. Generation and detection of reactive oxygen species in photocatalysis. *Chem. Rev.* **117**, 11302–11336 (2017).
48. Wang, Y. et al. Increasing solar absorption of atomically thin 2D carbon nitride sheets for enhanced visible-light photocatalysis. *Adv. Mater.* **31**, 1807540 (2019).
49. Tolosana-Moranchel, A., Casas, J. A., Carbajo, J., Faraldos, M. & Bahamonde, A. Influence of TiO_2 optical parameters in a slurry photocatalytic reactor: kinetic modelling. *Appl. Catal. B-Environ.* **200**, 164–173 (2017).
50. Grcic, I. & Puma, G. L. Six-flux absorption-scattering models for photocatalysis under wide-spectrum irradiation sources in annular and flat reactors using catalysts with different optical properties. *Appl. Catal. B-Environ.* **211**, 222–234 (2017).
51. Acosta-Herazo, R., Mueses, M. A., Puma, G. L. & Machuca-Martínez, F. Impact of photocatalyst optical properties on the efficiency of solar photocatalytic reactors rationalized by the concepts of initial rate of photon absorption (IRPA) dimensionless boundary layer of photon absorption and apparent optical thickness. *Chem. Eng. J.* **356**, 839–849 (2019).
52. Mena, E., Rey, A. & Beltrán, F. TiO_2 photocatalytic oxidation of a mixture of emerging contaminants: a kinetic study independent of radiation absorption based on the direct-indirect model. *Chem. Eng. J.* **339**, 369–380 (2018).
53. Perdew, J. P., Burke, K. & Wang, Y. Generalized gradient approximation for the exchange-correlation hole of a many-electron system. *Phys. Rev. B.* **54**, 16533 (1996).
54. Jiao, Y., Zheng, Y., Jaroniec, M. & Qiao, S. Z. Origin of the electrocatalytic oxygen reduction activity of graphene-based catalysts: a roadmap to achieve the best performance. *J. Am. Chem. Soc.* **136**, 4394–4403 (2014).
55. Nørskov, J. K. et al. Origin of the overpotential for oxygen reduction at a fuel-cell cathode. *J. Phys. Chem. B.* **108**, 17886–17892 (2004).

Acknowledgements

The authors thank the National Natural Science Foundation of China (52270149 and 51908528) and the Fundamental Research Funds for the Central Universities (2021CDJQY-014) for supporting this work. The authors also thank the related testers from Shiyanjia Lab (www.shiyanjia.com) for SEM measurements.

Author contributions

F. Chen and C.W. Bai conceived and planned the experiments, and C.W. Bai conducted the related experiments. F. Chen provided program support. P. J. Duan contributed to the DFT calculations. C.W. Bai conducted, and Z.Q. Zhang, Y.J. Sun, X.J. Chen, Q. Yang, and F. Chen assisted in collecting data and analyzing various characterizations. C.W. Bai, F. Chen, and H.Q. Yu wrote and revised the manuscript.

Competing interests

The authors declare no competing interests.

Additional information

Supplementary information The online version contains supplementary material available at https://doi.org/10.1038/s41467-024-52158-z.

Correspondence and requests for materials should be addressed to Fei Chen or Han-Qing Yu.

Peer review information *Nature Communications* thanks Hongwei Mi, and the other, anonymous, reviewer(s) for their contribution to the peer review of this work. A peer review file is available.